Metformin reverses early cortical network dysfunction and behavior changes in Huntington's disease

Isabelle Arnoux[1†], Michael Willam[2†], Nadine Griesche[3†], Jennifer Krummeich[2], Hirofumi Watari[1], Nina Offermann[3], Stephanie Weber[3], Partha Narayan Dey[4], Changwei Chen[5], Olivia Monteiro[5], Sven Buettner[3], Katharina Meyer[3], Daniele Bano[3], Konstantin Radyushkin[6], Rosamund Langston[5,6], Jeremy J Lambert[5], Erich Wanker[7], Axel Methner[4‡], Sybille Krauss[3‡*], Susann Schweiger[2‡*], Albrecht Stroh[1‡*]

[1]Institute of Pathophysiology, Focus Program Translational Neurosciences, University Medical Center, Mainz, Germany; [2]Institute for Human Genetics, University Medical Center, Mainz, Germany; [3]German Center for Neurodegenerative Diseases (DZNE), Bonn, Germany; [4]Department for Neurology, University Medical Center, Mainz, Germany; [5]Division of Neurosciences, Ninewells Hospital and Medical School, Dundee, United Kingdom; [6]Mouse Behavior Unit, University Medical Center, Mainz, Germany; [7]Department of Neuroproteomics, Max-Delbrück-Center, Berlin, Germany

*For correspondence:
Sybille.krauss@dzne.de (SK);
schweigs@uni-mainz.de (SS);
albrecht.stroh@unimedizin-mainz.de (AS)

†These authors contributed equally to this work
‡These authors also contributed equally to this work

Abstract Catching primal functional changes in early, 'very far from disease onset' (VFDO) stages of Huntington's disease is likely to be the key to a successful therapy. Focusing on VFDO stages, we assessed neuronal microcircuits in premanifest Hdh150 knock-in mice. Employing *in vivo* two-photon Ca^{2+} imaging, we revealed an early pattern of circuit dysregulation in the visual cortex - one of the first regions affected in premanifest Huntington's disease - characterized by an increase in activity, an enhanced synchronicity and hyperactive neurons. These findings are accompanied by aberrations in animal behavior. We furthermore show that the antidiabetic drug metformin diminishes aberrant Huntingtin protein load and fully restores both early network activity patterns and behavioral aberrations. This network-centered approach reveals a critical window of vulnerability far before clinical manifestation and establishes metformin as a promising candidate for a chronic therapy starting early in premanifest Huntington's disease pathogenesis long before the onset of clinical symptoms.
DOI: https://doi.org/10.7554/eLife.38744.001

Introduction

Huntington's disease is caused by the expansion of a CAG repeat in the open-reading frame of the huntingtin gene (*HTT*), which translates into an expanded glutamine stretch in the aberrant, mutant protein (mHTT). Huntington's disease has primarily been described as a late-onset neurodegenerative disease. However, it is preceded in its premanifest period by a prolonged presymptomatic phase followed by a prodromal phase with hardly detectable and unspecific symptoms occurring far before classical Huntington's disease becomes apparent (*Ross et al., 2014*). These symptoms include reduced impulse control, social disengagement, low conversational participation, reduction of the concentration span and decline of clearly defined cognitive domains (*Stout et al., 2011*; *Predict-HD Investigators of the Huntington Study Group et al., 2007*; *Ross et al., 2014*; *Labuschagne et al., 2016*) and are accompanied by slight changes of cortical

eLife digest Huntington's disease is a devastating brain disorder that causes severe mood disorders, problems with moving, and dementia. Most people develop the condition between their thirties and fifties, and die a decade or two after the symptoms first appear.

The disease emerges because of a mutation in the gene for the Huntingtin protein, which leads to neurons slowly dying in the brain. While genetic testing can reveal who carries the faulty gene, no treatment addresses the root of the disorder or prevents it from appearing. Instead, most therapies for Huntington's disease aim to reduce brain damage once the telltale symptoms are already present. However, the disease-causing protein is expressed early during the life of a patient, which could give it time to damage the brain long before neurons die and the disorder reveals itself. Treatments that start after the first signs of the disease may be too late to reverse the damage. Detecting and preventing early brain changes in people that carry the mutation may thus help to stop the disease from progressing.

Here, Arnoux, Willam, Griesche et al. set out to detect the minute changes that the faulty Huntingtin protein may cause in the brain network of young mice with the mutation. State-of-the-art imaging tools helped to examine individual neurons in the brain area that processes visual information. These experiments revealed that a group of brain cells had become hyperactive; once this change had occurred, the mutant animals were less anxious than is typical for mice.

Metformin is a drug used to treat diabetes, but it also interferes with a structure that is required to produce the disease-causing Huntingtin protein. Arnoux et al. therefore explored whether the compound could rescue the early brain alterations observed in mutant mice. Adding metformin in the water of the animals for three weeks halted the production of the mutant protein, reversed the brain changes and stopped the abnormal behavior.

Further work is now required in humans to confirm that Huntington's disease starts with a change in the activity of networks in the brain, and to verify that metformin can stop the disorder in its track.
DOI: https://doi.org/10.7554/eLife.38744.002

network topology and functional connectivity in resting state fMRI measures (*PREDICT-HD investigators of the Huntington Study Group et al., 2015*; *Wolf et al., 2012*). Importantly, such subtle network dysregulations may occur even earlier than the described prodromal symptoms in a very far from disease onset (VFDO) premanifest stage (*Figure 1a*). This stage reaches back more than 15–20 years before motor symptoms become visible in patients and far before protein aggregates and neurodegeneration are observed.

In Huntington's disease occurrence of such very early changes is supported by the observation of early deficits in premanifest Huntington's disease mutation carriers, such as loss of phosphodiesterase 10A in the occipital lobe up to 47 years prior to disease onset (summarized in *Wilson et al., 2017*). Also, the ability to perform complex visuospatial orientation, such as visual search, seems to be altered even in pre-manifest stages far from clinical diagnosis (*Labuschagne et al., 2016*). We hypothesize that primal functional changes in the VFDO stage of premanifest Huntington's disease open up very early vulnerable windows for disease development and preventive therapy prior to neuronal loss and may also provide promising early biomarkers for therapy development (*Mehler and Gokhan, 2000*; *Kerschbamer and Biagioli, 2015*; *Humbert, 2010*; *Cepeda et al., 2003*).

It seems that the visual cortex is one of the first regions that are functionally affected during disease development in Huntington's disease (*Labuschagne et al., 2016*; *Dogan et al., 2013*). In order to identify primal network changes, we have here established a network-centered approach and focused on microcircuit function in layer 2/3 of the visual cortex at an early premanifest stage in a mouse model of Huntington's disease corresponding to the VFDO stage in premanifest Huntington's disease. We have used two-photon imaging using fluorescent indicators of intracellular Ca^{2+} in order to resolve the functional architecture of intact cortical microcircuits *in vivo* with single neuron resolution (*Grienberger and Konnerth, 2012*). We show that even at the early age of 10 – 15 weeks (young adults compared to humans), the entire cortical microcircuit shifts towards a more excitable
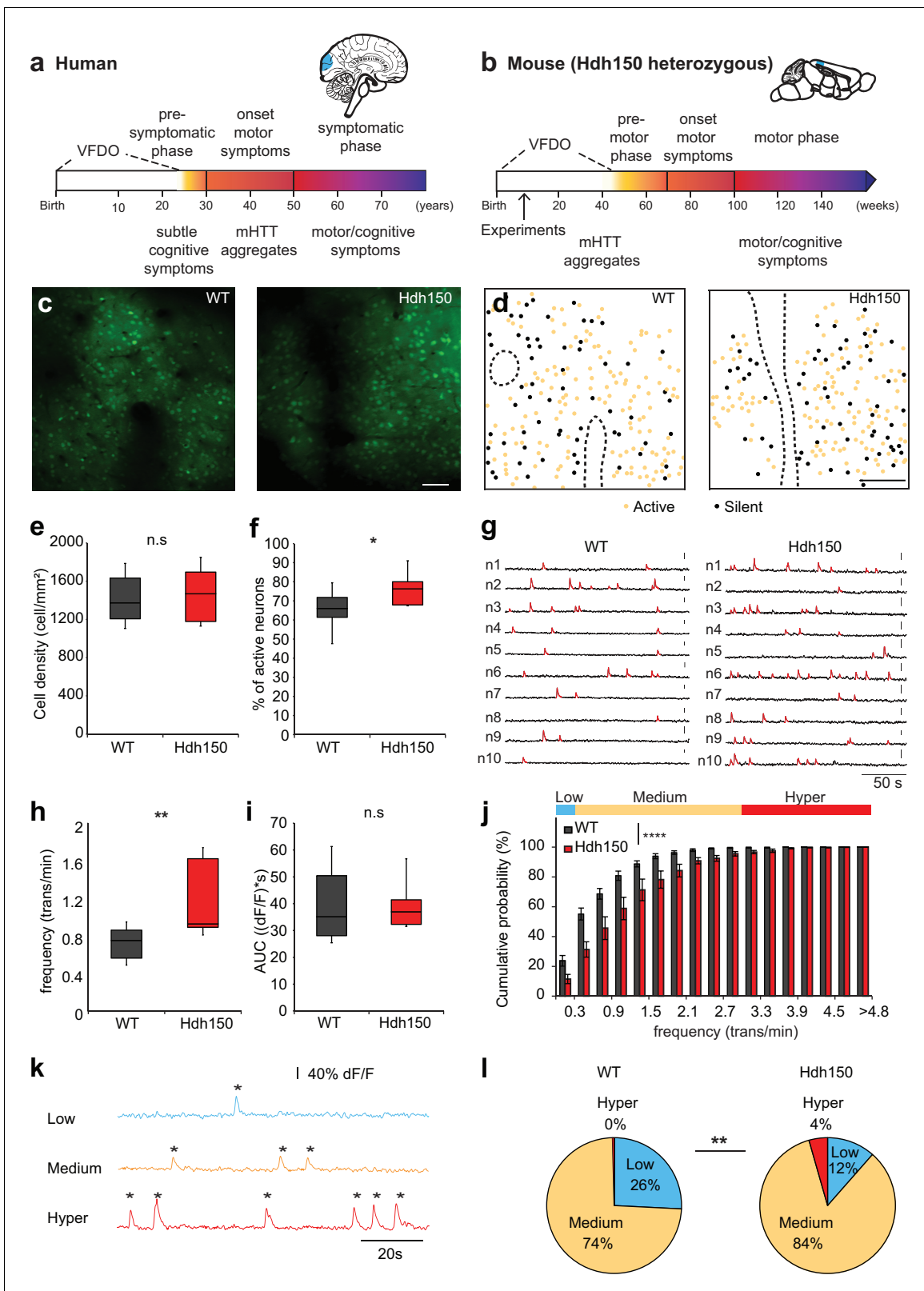
Figure 1. *In vivo* two-photon Ca^{2+} imaging in layer 2/3 of visual cortex reveals a hyperactive neuronal activity pattern prior to disease onset. (a,b) Top right, Illustrations indicating the visual cortex (blue area) in human (a) and mouse (b) brains. The brains are not drawn to scale. Bottom, timeline of Huntington's disease progression in human and Hdh150 mouse model of Huntington's disease. The Huntington's disease onset was age 30–50 years in humans and ~70 weeks in Hdh150 mice. We conducted our experiments during a very early pre-symptomatic phase, far prior to mHtt aggregates and

Figure 1 continued on next page

Figure 1 continued

motor symptoms. VFDO: very far from disease onset. (c) Representative two-photon images of OGB-1 AM staining in layer 2/3 of the visual cortex of WT and Hdh150 mice. Scale bar: 70 µm. (d) Color-coded maps of silent (black) and spontaneously active (orange) neurons in WT (left) and Hdh150 (right) mice. Dashed lines represent the boundaries of blood vessels (original images in *Figure 1c*). Scale bar: 100 µm. (e) Density of stained cells in layer 2/3 of the visual cortex in WT and Hdh150 mice. Unpaired t-test, p=0.71. (f) Increased proportion of spontaneously active neurons in Hdh150 mice. Unpaired t-test, p<0.05. (g) Representative traces of spontaneous Ca^{2+} transients (red) of 10 neurons recorded in vivo in WT and Hdh150 mice. Vertical scale bars: 40% dF/F. (h) Increased frequency of Ca^{2+} transients in spontaneously active neurons of Hdh150 mice. Silent neurons were excluded, as in subsequent panels. Mann-Whitney test, p<0.01 (i) Quantification of area under the curve (AUC) of Ca^{2+} transients. Unpaired t-test, p=0.98 (j) Cumulative frequency distribution of Ca^{2+} transients in WT (dark grey) and Hdh150 (red) mice. Top, colored categorization of neurons according to their Ca^{2+} transient frequencies. Two-way ANOVA, group: p<0.0001, time: p<0.0001, Interaction: p<0.0001. (k) Color-coded categorization of neurons according to their Ca^{2+} transient frequency: 'low' (<0.3 trans/min, blue; silent neurons excluded), 'medium' (0.3–3 trans/min, orange) and 'hyper' (>3 trans/min, red). Each peak is marked by an asterisk. (l) Relative proportion of low, medium and hyperactive neurons in layer 2/3 of the visual cortex in WT (left) and Hdh150 (right) mice. Chi-square test, p<0.01.

DOI: https://doi.org/10.7554/eLife.38744.003

The following video, source data, and figure supplements are available for figure 1:

Source data 1. Numerical values of *Figure 1* and associated supplement figures.

DOI: https://doi.org/10.7554/eLife.38744.007

Source data 2. Code used for the analysis of calcium imaging.

DOI: https://doi.org/10.7554/eLife.38744.008

Figure supplement 1. Ca^{2+} events from astrocytes and neurons show clearly distinct kinetics.

DOI: https://doi.org/10.7554/eLife.38744.004

Figure supplement 2. Cortical hyperactivity is independent of mHtt aggregation, astrogliosis or apoptotic cell death in presymptomatic VFDO Hdh150 mice.

DOI: https://doi.org/10.7554/eLife.38744.005

Figure supplement 3. Randomization of experimental data to assess specific spatial clustering.

DOI: https://doi.org/10.7554/eLife.38744.006

Figure 1—video 1. *In vivo* two-photon images of mouse visual cortex performed at different depths (indicated in the upper left corner) after multi-bolus loading with OGB-1 AM.

DOI: https://doi.org/10.7554/eLife.38744.009

Figure 1—video 2. Representative time-lapse of *in vivo* two-photon Ca^{2+} imaging acquired in layer 2/3 of mouse visual cortex showing single-cell Ca^{2+} transients.

DOI: https://doi.org/10.7554/eLife.38744.010

state characterized by a complex change in neuronal activity pattern and hyperactive neurons. These findings are accompanied by changes in animal behavior, including a decrease in anxiety.

No effective and curative treatment has been developed for Huntington's disease so far (*Frank, 2014*). A chronic drug therapy that commences early on in VFDO stages in premanifest Huntington's disease and ameliorates early dysregulations as the potential origin of pathogenic processes and disease spreading is therefore a promising and necessary strategy. In Huntington's disease animal models, even short-term reduction of protein load through RNA interference and antisense strategies has beneficial effects on disease phenotypes and progression lasting several months after intervention (*Stanek et al., 2014*; *DiFiglia et al., 2007*; *Keiser et al., 2016*). We have recently shown that mRNAs carrying CAG repeats bind to a protein complex containing the ubiquitin ligase midline 1 (MID1) in a repeat size-dependent manner. Through ubiquitination MID1 regulates PP2A (protein phosphatase 2A) and mTOR (mechanistic target of rapamycin) activities and the translation of associated mRNAs (*Krauss et al., 2013*; *Griesche et al., 2016*). Disruption of the MID1/PP2A/mTOR protein complex leads to an increase of PP2A activity, a decrease of mTOR activity and a reduction of translation rates of mRNAs with expanded CAG repeats (*Krauss et al., 2013*).

We show here that the type II diabetes drug metformin interferes with the MID1/PP2A/mTOR protein complex and significantly reduces the translation rate of *Htt* mRNA, resulting in a reduction of aberrant Htt protein production *in vitro* and *in vivo* in the Hdh150 mouse model. Notably, in Hdh150 mice *in vivo* metformin, when given early in the VFDO stage, and chronically in the drinking water, fully reverses both early neuronal network dysregulations and behavioral aberrations.

Results

Increase in cortical neuronal network activity in presymptomatic Huntington's disease mice

Since the visual cortex is one of the first regions affected by the disease (*Dogan et al., 2013*; *Labuschagne et al., 2016*), we focused on layer 2/3 of the visual cortex of ~12 weeks old, heterozygous knock-in mice expressing expanded Htt with 150 glutamine repeats (Hdh150), in the lightly anesthetized mouse. This time corresponds to the VFDO in presymptomatic Huntington's disease (*Figure 1a,b*). We focused our analysis on male mice, thereby minimizing the influence of hormonal fluctuations on network activity. This approach is in line with a recent study in the field of Alzheimer's disease (*Iaccarino et al., 2016*), using males only. We employed two-photon Ca^{2+} imaging *in vivo* using the synthetic Ca^{2+} indicator Oregon-Green BAPTA1 (OGB-1) AM to monitor the suprathreshold activity of a neuronal microcircuit with cellular resolution, typically comprising around 200 neurons (*Kerr et al., 2005*) (*Figure 1c*, *Figure 1—figure supplement 1a,b*). Events from astrocytes, which are also stained by OGB-1, were excluded from this neuronal network based on their temporal dynamics (*Figure 1—figure supplement 1c–f*, *Figure 1—source data 1*).

By imaging at different depths, we found a similar spatial extent of OGB-1 staining in the visual cortex of Hdh150 and control wild-type (WT) mice (*Figure 1—figure supplement 1b*). *Figure 1—video 1* shows two-photon images acquired from the pial surface illustrating a homogenous OGB-1 staining in layers 1, 2 and 3 of mouse visual cortex. We observed no difference in the density of stained cells (*Figure 1c and e*, *Figure 1—source data 1*, WT: 1413 ± 74 cells/mm^2 (n = 11 mice), Hdh150 1456 ± 90 cells/mm^2 (n = 10 mice), Mann-Whitney test p=0.8).

To identify changes in microcircuit activity, we assessed spontaneous activity *in vivo* in the cortical microcircuit of WT and Hdh150 mice, which reliably reflects the functional microarchitecture of sensory cortical areas (*Miller et al., 2014*). *Figure 1—video 2* shows an example of *in vivo* two-photon Ca^{2+} imaging exhibiting ongoing spontaneous activity in layer 2/3 of mouse visual cortex with single-cell resolution. Both WT and Hdh150 mice exhibited silent and active cells (*Figure 1d*), but a significantly higher proportion of active neurons was detected in Hdh150 mice, indicating a more active network (*Figure 1f*, *Figure 1—source data 1*, WT: $65.1 \pm 3.5\%$ (n = 8 mice), Hdh150: $77.1 \pm 3.5\%$ (n = 6 mice), unpaired t-test p<0.05). No spatial clustering of silent or active cells could be observed in either group (*Figure 1d*).

Next, we analyzed the frequency of Ca^{2+} transients and activity patterns in the population of active neurons (*Figure 1—source data 2*). Notably, the frequency of Ca^{2+} transients was significantly higher in Hdh150 compared to WT mice (*Figure 1g–h*, *Figure 1—source data 1*, WT: 0.74 ± 0.06 trans/min (n = 8 mice), Hdh150: 1.2 ± 0.14 trans/min (n = 6 mice), Mann-Whitney test, p<0.01). No difference was found in the mean area under the curve (AUC) of Ca^{2+} transients between WT and Hdh150 mice (*Figure 1i*, *Figure 1—source data 1*, WT: 39.8 ± 3.9 (dF/f)*s, Hdh150: 39.9 ± 3.6 (dF/f)*s, unpaired t-test, p=0.98) indicating that on average, the mean number of underlying action potentials for each individual calcium transient was not different in Hdh150 mice.

We furthermore analyzed the distribution of neurons according to their Ca^{2+} transient frequency. The cumulative probability distribution of the activity of individual neurons in Huntington's disease mice was shifted toward higher frequencies indicating that the overall neuronal activity transitioned toward a more excitable network (*Figure 1j*, *Figure 1—source data 1*, two-way ANOVA p<0.0001). We sub-classified the active neurons into three functional subgroups according to their transient frequency: low, medium and hyperactive (*Figure 1k*, *Figure 1—source data 1*). Notably, we identified a unique subgroup in VFDO Hdh150 mice: hyperactive neurons (*Figure 1l*, *Figure 1—source data 1*, Chi-square test p<0.01). This subgroup was accompanied by a reduction in the number of neurons with low activity, which corroborates the shift of the microcircuit activity.

In later stages of Alzheimer's disease, hyperactive cells were shown to cluster near amyloid plaques (*Busche et al., 2008*). A similar scenario might occur in Huntington's disease. To clarify whether the cortex of VFDO Hdh150 mice is affected by mHtt aggregates - a later stage Huntington's disease hallmark - we performed immunohistochemistry in Hdh150 and WT animals. We observed only diffuse and non-aggregated Htt immunoreactivity in the cytoplasm of neurons in cortical areas of both WT and Hdh150 mice (*Figure 1—figure supplement 2a*) in accordance with previous studies (*Lin et al., 2001*). In addition, no reactive astrocytes were observed (*Figure 1—figure supplement 2b*) and only few cells that were stained for activated caspase-3, an apoptotic marker, in cortical

areas of WT and Hdh150 mice (*Figure 1—figure supplement 2c*) as previously observed (*Yu et al., 2003*). In order to test whether hyperactive cells cluster in the Hdh150 mouse model, spatial distance between every pair of neurons was quantified (*Figure 1—figure supplement 3c,d*, *Figure 1—source data 1*). We observed no significant differences between the permutations of functional subgroups in premanifest Hdh150 and control mice, reflecting a rather homogenous distribution of all functional subgroups (*Figure 1—figure supplement 3c,d*, *Figure 1—source data 1*, Mann-Whitney, not significant, see *Table 1* for p-values). This finding was confirmed in randomized data in which cell location was kept but functional identity was randomly permutated (*Figure 1—figure supplement 3a,b and d*, *Figure 1—source data 1*). Taken together, clustering of hyperactive cells could not be observed in VFDO Hdh150 animals and cortical hyperactivity is independent of mHtt aggregation, apoptotic cell death or astrogliosis at this presymptomatic VFDO stage.

Increased synchronicity and cortical dysfunction in premanifest VFDO Huntington's disease mice

An important aspect of neuronal information processing is the optimization of encoding strategies. In the visual cortex, encoding of information is characterized by sparse and precisely timed neuronal activity. Cortical activity is defined by transiently co-active ensembles of neurons acting as a functional unit (*Miller et al., 2014*). To capture these spatiotemporal dynamics in the microcircuit, we analyzed synchronicity of the transients between all pairs of neurons (*Figure 2a*) by calculating Pearson's correlation coefficient (Pearson's r) for every pair. First, we confirmed that the level of synchronicity within a healthy cortical microcircuit is drastically higher than the random synchronicity in shuffled data (*Figure 2b*, *Figure 2—source data 1*, WT: 0.024 ± 0.005, WT rand: -0.0003 ± 0.0003, Mann-Whitney test $p<0.0001$). Notably, the synchronicity was even higher in Hdh150 mice compared to healthy controls (*Figure 2b*, *Figure 2—source data 1*, WT: 0.02 ± 0.005, Hdh150: 0.04 ± 0.006, Mann-Whitney test $p<0.05$).

Next, we compared the synchronicity level in all functional subgroups (*Figure 2c*, *Figure 2—source data 1*). The pairs involving the low activity subgroups (LL and LM) showed no differences in WT and Hdh150 mice (Mann-Whitney test, in LL $p=0.5$ and in LM $p=0.7$). However, Pearson's r increased significantly for the medium-to-medium (MM) pairs in Hdh150. Pearson's r was even higher for medium-hyperactive (MH) and hyperactive-hyperactive (HH) compared to low-low (LL) pairs (Mann-Whitney test compared to LL in Hdh150 mice: in MM $p<0.05$, in MH and HH $p<0.01$).

To assess whether the increased synchronicity in the VFDO Hdh150 mice occurred merely due to the higher number of transients, we used randomized data with unchanged frequency but temporally shuffled transients (*Figure 1—figure supplement 3a and b*). Pearson's r in the randomized data was nearly zero for all, including the high frequency subgroups in WT and Hdh150 mice (*Figure 2—figure supplement 1a and b*, *Figure 2—source data 1*). This finding argued against the possibility that the increased Pearson's r in the experimental data occurred by chance.

We next asked whether functional ensembles with a high level of synchronicity are located in spatial vicinity to each other, by testing whether Pearson's r changed with physical distance between the pairs of neurons (*Figure 2d*). An inverse linear relationship was observed between Pearson's r and the pairwise distance in both the WT and Hdh150 mice (*Figure 2d*, *Figure 2—source data 1*, two-way ANOVA $p<0.0001$, WT vs Hdh150) suggesting that two closely located neurons have a higher probability to fire together. This is consistent with similar findings in the forelimb motor cortex of head-restrained mice (*Dombeck et al., 2009*). Randomization of the data abolished the inverse relationship between Pearson's r and distance (*Figure 2e*, *Figure 2—source data 1*, two-way ANOVA $p=0.3$, WT rand vs Hdh150 rand).

Since many studies, especially in premanifest mutation carriers, have linked Huntington's disease pathology to changes in metabolism (*Damiano et al., 2010*; *Duan et al., 2014*; *Jin and Johnson, 2010*; *Labbadia and Morimoto, 2013*; *Mochel and Haller, 2011*), hyperactivity might mirror metabolic dysregulation in subgroups of cortical cells. We used mitochondrial respiration as a marker of metabolic functionality and quantified mitochondrial respiration using high-resolution respirometry of cortical tissues. Mitochondrial respiration was unchanged in cortical tissue of Hdh150 mice suggesting that the observed neuronal hyperactivity occurs prior to metabolic changes (*Figure 2—figure supplement 2a–c*, *Figure 2—source data 1*, Mann-Whitney test, not significant, see *Table 1* for p-values).

Table 1. Statistics

Figure	Test	Values	N
Figure 1e	Unpaired t test, two-tailed	NS, p=0.71	WT n = 11 mice; Hdh150 n = 10 mice
Figure 1f	Unpaired t test, two-tailed	p=0.023	WT n = 1204 cells in eight mice; Hdh150 n = 933 cells in six mice
Figure 1h	Mann-Whitney test	p=0.006	WT n = 765 cells in eight mice; Hdh150 n = 695 cells in six mice
Figure 1i	Unpaired t test, two-tailed	NS, p=0.98	WT n = 765 cells in eight mice; Hdh150 n = 695 cells in six mice
Figure 1j	Two-way ANOVA test	Group: p<0.0001, Df = 1, F = 85.96, time: p<0.0001, Df = 16, F = 147, Interaction: p<0.0001, F = 4.9, Df = 16	WT n = 765 cells in eight mice; Hdh150 n = 695 cells in six mice
Figure 1l	Chi-square test	p=0.002, df = 1, Chi-square = 9.127	WT n = 765 cells in eight mice; Hdh150 n = 695 cells in six mice
Figure 2b	Mann-Whitney test	WT vs Hdh150 p=0.03; WT vs WT rand p<0.0001; Hdh150 vs Hdh150 rand p<0.0001	WT n = 26126 Pearson's r in eight mice; Hdh150 n = 58050 Pearson's r in six mice
Figure 2c	Mann-Whitney test	WT vs Hdh150 mice: MM p=0.041 in Hdh150 mice; compared to LL: MM p=0.0496, MH p=0.005, HH p=0.009	WT n = 26126 Pearson's r in eight mice; Hdh150 n = 58050 Pearson's r in six mice
Figure 2d	Two-way ANOVA test	Group: p<0.0001, Df = 1, F = 58.20 Distance: p=0.97, Df = 15, F = 0.44 Interaction: p=0.33, df = 15, F = 1.13	WT n = 26126 distances in eight mice; Hdh150 n = 58050 distances in six mice
Figure 2e	Two-way ANOVA test	p=0.35, Df = 1, F = 0.86	WT rand n = 26126 distances in eight mice; Hdh150 rand n = 58050 distances in six mice
Figure 3b	Mann-Whitney test	p=0.031119	WT n = 10 mice; Hdh150 n = 13 mice
Figure 4a	Mann-Whitney test	control vs 1 mM metformin p=0.084521, control vs 2.5 mM metformin p=0.023231	Control n = 10, 1 mM metformin n = 11, 2.5 mM metformin n = 10.
Figure 4b	Mann-Whitney test	control siRNA vs MID1 siRNA p=0.008, control siRNA vs MID1 siRNA + metformin p=0.015	Control siRNA n = 6, MID1 siRNA n = 6, MID1 siRNA + metformin n=6.
Figure 4c	RM two-way ANOVA	Treatment: p=0.0082, Df = 2, F = 5 Time: p<0.0001, Df = 47, F = 27.5 Interaction: p<0.0001, Df = 94, F = 5.9	$n_{control}$ = 47, $n_{metformin\ 1mM}$ = 44, $n_{metformin\ 2.5mM}$ = 35
Figure 4d	RM two-way ANOVA	Treatment: p=0.0021, Df = 3, F = 5.1 Time: p<0.0001, Df = 47, F = 64.1 Interaction: p<0.0001, Df = 141, F = 6.1 p<0.0001	$n_{control}$ = 46, $n_{metformin}$ = 49, $n_{metformin+OA}$ = 51, n_{OA} = 43
Figure 4f	Unpaired t-test	p=0.0473	Hdh150 n = 6; Hdh150 metformin n = 6
Figure 4h	Unpaired t-test	p=0.0467	Hdh150 n = 3; Hdh150 metformin n = 3

Table 1 continued on next page

Table 1 continued

Figure	Test	Values	N
Figure 4i	Unpaired t-test	p=0.0062	Hdh150 n = 3; Hdh150 metformin n = 3
Figure 4j	Unpaired t-test	p=0.8766	Hdh150 n = 3; Hdh150 metformin n = 3
Figure 5b	Mann-Whitney test	WT vs Hdh150 p=0.023, Hdh150 vs Hdh150 met p=0.03, Hdh150 vs WT met p=0.012	WT n = 1204 cells in eight mice; Hdh150 n = 933 cells in six mice; WT met n = 1915 cells in nine mice; Hdh150 met n = 1585 cells in six mice
Figure 5c	Mann-Whitney test	WT vs Hdh150 p=0.006; Hdh150 vs Hdh150 met p=0.007; Hdh150 vs WT met p=0.008	WT n = 765 cells in eight mice; Hdh150 n = 695 cells in six mice; WT met n = 1199 in nine mice; Hdh150 met n = 1014 cells in six mice
Figure 5d	Two-way ANOVA test	Group: p<0.0001, Df = 3, F = 61.80 Time: p<0.0001, Df = 16, F = 345.9 Interaction: p<0.0001, Df = 48, F = 3.64	WT n = 765 cells eight mice; Hdh150 n = 695 cells six mice; WT met n = 1199 cells nine mice; Hdh150 met n = 1012 cells six mice
Figure 5e	Chi-square test	p=0.62, df = 1; Chi-square = 0.24	WT n = 765 cells eight mice; Hdh150 n = 695 cells six mice; WT met n = 1199 cells nine mice; Hdh150 met n = 1012 cells six mice
Figure 5f	Mann-Whitney test	WT vs Hdh150 p=0.03; Hdh150 vs Hdh150 met p=0.002; Hdh150 vs WT met p=0.003	WT n = 765 cells eight mice; Hdh150 n = 695 cells six mice; WT met n = 1199 cells nine mice; Hdh150 met n = 1012 cells six mice
Figure 5g	Two-way ANOVA test	Group: p<0.0001, Df = 3, F = 85.96 Distance: p=0.99, Df = 45, F = 0.58 Interaction: p=0.0007, Df = 15, F = 2.63	WT n = 765 cells eight mice; Hdh150 n = 695 cells six mice; WT met n = 1199 cells nine mice; Hdh150 met n = 1012 cells six mice
Figure 5i	Mann-Whitney test	WT vs Hdh150 p=0.002, Hdh150 vs Hdh150 Met p=0.002, Hdh150 vs. WT met p=0.02, WT vs Hdh150 Met p=0.82	WT n = 10; Hdh150 n = 13; WT met n = 6; Hdh150 met n = 8 mice
Figures supplements	Test	values	n
Figure 1—figure supplement 1e	Mann-Whitney test	p=0.002	n = 6 neurons, n = 6 astrocytes
Figure 1—figure supplement 1f	Mann-Whitney test	p=0.002	n = 6 neurons, n = 6 astrocytes

Table 1 continued on next page

Table 1 continued

Figure	Test	Values	N
Figure 1—figure supplement 3d	Mann-Whitney test	In WT mice: SS vs SL p=0.5, SS vs SM p=0.9, SS vs LL p=0.1, SS vs LM p=0.2, SS vs MM p=0.1, SL vs SM p=0.4, SM vs LL p=0.1, SM vs MM p=0.1, LL vs MM p=0.9, LM vs MM p=0.4, LM vs SM, p=0.2. In Hdh150 mice: SS vs SL p=0.8, SS vs SM p=0.5, SS vs SH p=0.9, SS vs SH p=0.9, SS vs LL p=0.9, SS vs LM p=0.9, SS vs LH p=1, SS vs MM p=0.1, SS vs MH p=0.1, SS vs HH p=0.4, SL vs SM p=0.8, SL vs SH p=0.9, SL vs LL p=0.9, SL vs LM p=0.9, SL vs LH p=0.8, SL vs MM p=0.5, SL vs MH p=0.6, SL vs HH p=0.7, SN vs SH p=0.6, SM vs LL p=0.7, SM vs LM p=0.6, SN vs LH p=0.4, SM vs MM p=0.3, SN vs MH p=0.4, SN vs HH p 0 0.6, SH vs LL p=0.7, SH vs LM p=1, SH vs LH p=1, SH vs MM p=0.4, SH vs MH p=0.3, SH vs HH p=0.6, LL vs LM p=0.9, LL vs LH p=1, LL vs MM p=0.5, LL vs MH p=0.7, LL vs HH p=0.8, LM vs LH p=0.6, LM vs MM p=0.3, LM vs MH p=0.3, LM vs HH p=0.5, LH vs MM p=0.3, LH vs MH p=0.3, LH vs HH p=0.5, MM vs MH p=0.7, NN vs HH p=0.8, MH vs HH p=0.9 In WT vs WT rand: WT mice: SS p=0.5, SL p=0.7, SM p=0.3, LL p=0.3, LM p=0.8, MM p=0.1. In Hdh150 vs Hdh150 rand: SS p=0.6, SL p=1, SM p=1, SH p=0.6, LL p=0.7, LM p=0.6, LH p=0.2, MM p=0.6, MH p=0.8, HH p=0.7 NS	WT n = 72595 distances eight mice; Hdh150 n = 132009 distances six mice
Figure 2—figure supplement 1a	Mann-Whitney test	LL p=0.005; LM p<0.0001; MM p<0.0001	WT n = 26126 Pearson's r in eight mice
Figure 2—figure supplement 1b	Mann-Whitney test	LL p=0.004; LM p=0.0006; LH p=0.041; MM p<0.0001; MH p=0.0002; HH p=0.01. In Hdh150 mice, compared to LL: MM p=0.049; MH p=0.005; HH p=0.009	Hdh150 n = 58050 Pearson's r in six mice
Figure 2—figure supplement 2c	Mann-Whitney test	routine p=0.4, leak p=0.5, CI p=0.6, CI + CII p=0.5, ETS p=0.2	WT n = 6 mice; Hdh150 n = 6 mice
Figure 3—figure supplement 1b	RM two-way ANOVA	Genotype: p=0.6, Df = 1, F = 0.3 Time: p<0.0001, Df = 6, F = 86.1 Interaction: p=0.6, Df = 6, F = 0.7	WT n = 16 mice; Hdh150 n = 13 mice
Figure 3—figure supplement 1c	RM two-way ANOVA	Genotype: p=0.5, Df = 1, F = 0.5 Time: p<0.0001, Df = 9, F = 35.4 Interaction: p=0.03, Df = 9, F = 2.2	WT n = 16 mice; Hdh150 n = 13 mice
Figure 3—figure supplement 1d	RM two-way ANOVA	Genotype: p=0.8, Df = 1, F = 3.4 Time: p<0.01, Df = 6, F = 3.4 Interaction: p=0.97, Df = 6, F = 0.2	WT n = 16 mice; Hdh150 n = 13 mice
Figure 3—figure supplement 1e	Mann-Whitney test	p=0.3	WT n = 10; Hdh150 n = 13; WT met n = 6; Hdh150 met n = 8 mice
Figure 4—figure supplement 1a	RM two-way ANOVA	Treatment p=0.0342, Df = 2, F = 3.5; Time p<0.0001, Df = 47, F = 45.3; Interaction p<0.0001, Df = 94, F = 3.5	$n_{control}$ = 36, $n_{metformin\ 1mM}$ = 42, $n_{metformin\ 2.5mM}$ = 44
Figure 4—figure supplement 1b	RM two-way ANOVA	Treatment p=0.2986, Df = 1, F = 1.9; Time p=0.0654, Df = 20, F = 1.8; Interaction p=0.9988, Df = 20, F = 0.3.	control n = 7, metformin n = 8
Figure 4—figure supplement 1dc	Unpaired t-test	p=0,1826	Hdh150 n = 4; Hdh150 metformin n = 4
Figure 4—figure supplement 2a	Mann-Whitney test	p<0.0001	control n = 65, metformin n = 65
Figure 4—figure supplement 2b	Mann-Whitney test	Q40 vs. Q40 Met p<0.0001	Q40 n = 43, Q40 Met n = 43
Figure 4—figure supplement 2c	Mann-Whitney test	Ctrl vs. 5 mM p=0.0078, Ctrl vs. 10 mM p<0.0001	n = 45
Figure 4—figure supplement 2d	Mann-Whitney test	p<0.0001	Control n = 72, arc-1 RNAi n = 74
Figure 4—figure supplement 2e	Mann-Whitney test	p<0.0001	Control n = 60, arc-1 RNAi n = 62
Figure 5—figure supplement 1b	Unpaired t test, two-tailed	WT met vs. Hdh150 met p=0.39, WT vs. WT met p=0.7, Hdh150 vs. Hdh150 met p=0.9	WT n = 11; Hdh150 n = 10; WT met n = 9; Hdh150 met n = 6 mice

Table 1 continued on next page

Table 1 continued

Figure	Test	Values	N
Figure 5—figure supplement 1c	Unpaired t test, two-tailed	WT vs WT met p=0.024	WT n = 765 cells eight mice; Hdh150 n = 695 cells six mice; WT met n = 1199 cells nine mice; Hdh150 met n = 1012 cells six mice
Figure 5—figure supplement 1d	Unpaired t test, two-tailed	WT met: LL vs LM p=0.04 and LL vs MM p<0.0001; Hdh150 met: LL vs LM p=0.4, LL vs MM p=0.004	WT met n = 57140 Pearson's r in nine mice; Hdh150 met n = 49535 Pearson's r in six mice
Figure 5—figure supplement 1e	Mann-Whitney test	LM WT vs LM Hdh150; MM WT vs MM Hdh150 p=0.04	WT n = 26126 Pearson's r in eight mice; Hdh150 n = 58050 Pearson's r in six mice; WT met n = 57140 Pearson's r in nine mice; Hdh150 met n = 49535 Pearson's r in six mice
Figure 5—figure supplement 1f	Mann-Whitney test	SS p=0.1, SL p=0.1, SM p=0.1, LL p=0.4, LM p=0.3, MM p=0.2	WT met n = 140467 distances in nine mice; Hdh150 met n = 117485 distances in six mice

Behavior changes in premanifest VFDO Huntington's disease mice

Next, we asked whether hyperactivity and increased synchronicity of cortical networks are associated with behavioral changes in the VFDO animals. A visual discrimination task did not show any aberrations in the Hdh150 animals (*Figure 3—figure supplement 1a–d*; *Figure 3—video 1*, *Figure 3—source data 1*, two-way ANOVA, not significant, see *Table 1* for p-values). In contrast, in an open-field test premanifest VDFO Hdh150 animals moved significantly more to the center than WT littermates suggesting anxiolytic effects of the VFDO changes (*Figure 3a,b*, *Figure 3—source data 1*, Mann-Whitney test, p=0.03). Distance travelled (as a measure of motility) did not differ between groups (*Figure 3—figure supplement 1e*, *Figure 3—source data 1*, Mann-Whitney test, not significant, see *Table 1* for p-values).

Taken together, we have found network hyperactivity in the cortex of VFDO Hdh150 mice combined with anxiolytic behavior.

Metformin reduces mutant Htt protein load

Based on our previous observations that the MID1/PP2A/mTOR protein complex regulates the translation of mHtt protein (*Krauss et al., 2013*) and that treatment with metformin interferes with the MID1 complex (*Kickstein et al., 2010*), we hypothesized that metformin inhibits the MID1/PP2A/mTOR-mediated protein synthesis of mutant mHtt and is therefore a promising candidate molecule to reduce mHtt load and reverse symptoms associated with Huntington's disease.

In order to test for an effect of metformin on mHtt protein load and aggregation, HEKT cells stably expressing FLAG-tagged exon 1 of human mHTT carrying 83 CAG repeats were treated with 1 mM or 2.5 mM metformin, or with vehicle for 48 hr. Aggregation was quantified in a filter retardation assay. Metformin reduced the amount of aggregated FLAG-HTT in a concentration-dependent manner (*Figure 4a*, *Figure 4—source data 1*, Mann-Whitney test, control vs 2.5 mM metformin p=0.02).

To test whether the metformin effect on human exon 1 mHTT aggregates is mediated by a blockade of the MID1 protein complex, we depleted MID1 by siRNA-mediated knockdown in the cell line expressing FLAG-HTT exon 1 with 83 CAG repeats, in presence or absence of metformin. While depletion of MID1 reduced mHTT aggregation, no additive effect of metformin treatment on mHTT
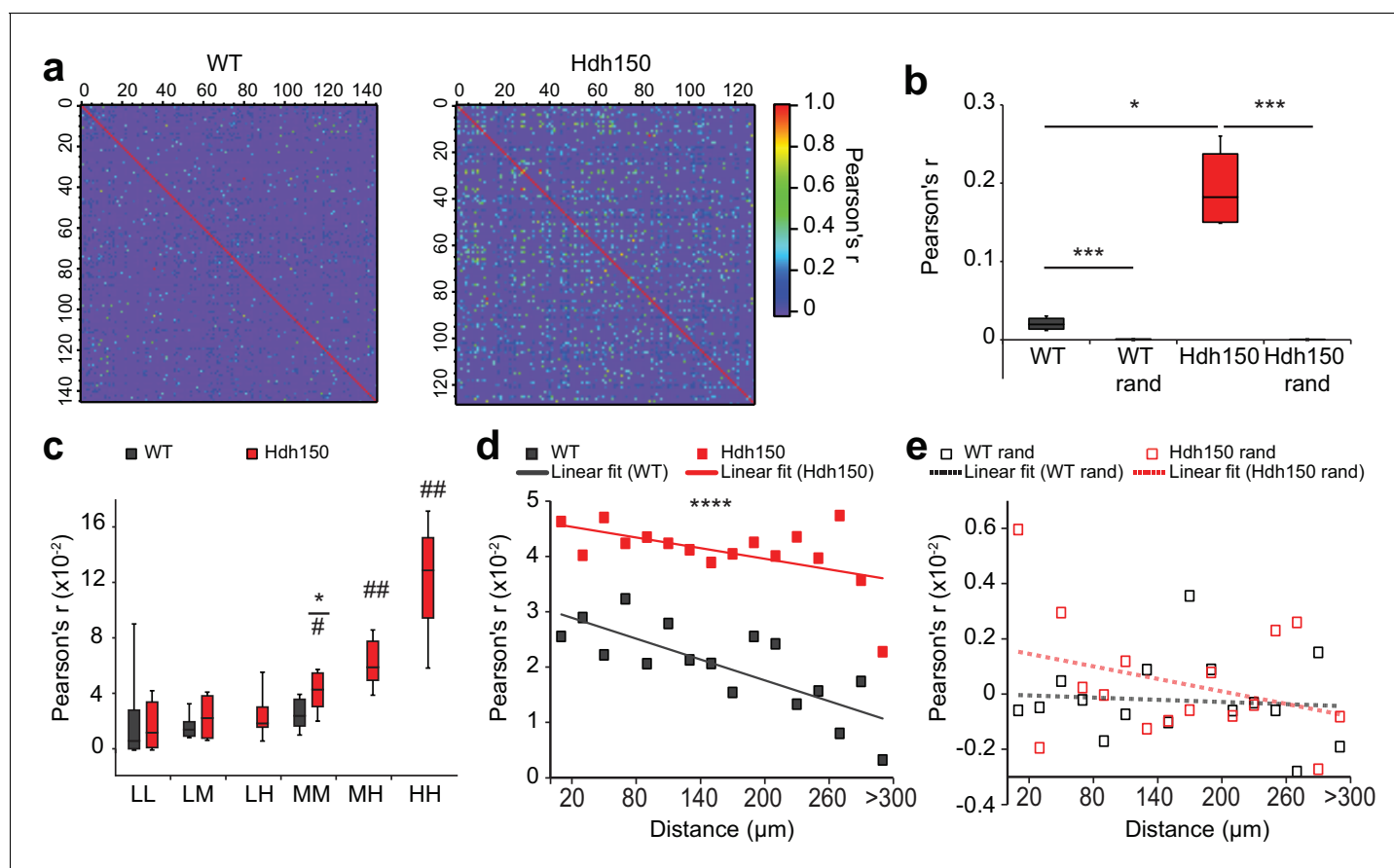
Figure 2. Presymptomatic Hdh150 mice exhibit an increased synchronicity of cortical microcircuits. (**a**) Color-coded Pearson's r matrices calculated from representative recordings of WT (left) and Hdh150 (right) mice. Silent cells were excluded from the analysis. Right, color-coded scale of Pearson's r values. (**b**) Overall Pearson's correlation coefficient (Pearson's r) in WT (dark grey) and Hdh150 (red) mice for experimental (filled) and randomized (open) raster data. Mann-Whitney test, WT vs. Hdh150 p<0.05; WT vs. WT rand p<0.0001; Hdh150 vs. Hdh150 rand p<0.0001 (**c**) Pearson's r for combinations of neuronal pairs (LL: low-low, LM: low-medium, LH: low-hyper, MM: medium-medium, MH: medium-hyper, HH: hyper-hyper) in WT (dark grey) and Hdh150 (red) mice. * pairwise comparisons between a pair of WT and Hdh150 mice. # comparisons of functional subgroup pairs to the low-low pair within the same genotype. The pairs involving hyperactive neurons could only be analyzed in Hdh150 mice. Mann-Whitney test, WT vs. Hdh150 mice: MM p<0.05 in Hdh150 mice; compared to LL: MM p<0.05, MH p<0.01, HH p<0.01 (**d,e**) Relationship between Pearson's r and distance between neuronal pairs in WT (black) and Hdh150 (red) mice (**d**) and randomized data (**e**). Lines represent the linear fit of WT and Hdh150 experimental data. Two-way ANOVA (**d**) Genotype: p<0.0001 Distance: p=0.97, Interaction: p=0.3, (**e**) Genotype = 0.35, p=0.3, Interaction: p=0.8.

DOI: https://doi.org/10.7554/eLife.38744.012

The following source data and figure supplements are available for figure 2:

Source data 1. Numerical values of *Figure 2* and associated supplement figures.
DOI: https://doi.org/10.7554/eLife.38744.015

Figure supplement 1. Randomization of experimental data to assess specific network synchronicity.
DOI: https://doi.org/10.7554/eLife.38744.013

Figure supplement 2. Presymptomatic Hdh150 mice did not exhibit alteration of mitochondria respiration.
DOI: https://doi.org/10.7554/eLife.38744.014

aggregates was observed, suggesting that MID1 and metformin indeed act through the same pathway (*Figure 4b*, *Figure 4—source data 1*, Mann-Whitney test, control siRNA vs MID1 siRNA p=0.009; control siRNA vs MID1 siRNA +metformin p=0.02).

We had shown previously that the MID1/PP2A/mTOR protein complex regulates the translation efficiency of the human *HTT* mRNA in a repeat-dependent manner (*Krauss et al., 2013*). We therefore looked at a possible influence of metformin on the protein synthesis rate of mHTT exon one protein using a previously described FRAP (Fluorescence recovery after photo bleaching) - based assay that allows monitoring of protein translation rates in living cells (*Krauss et al., 2013*). We

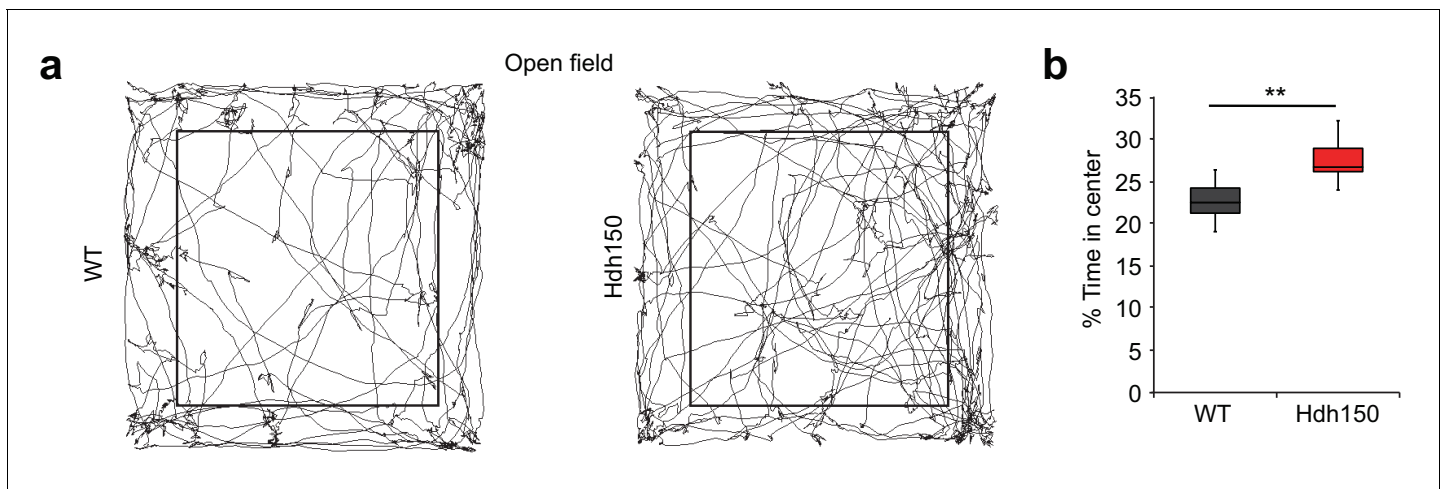**Figure 3.** Presymptomatic VFDO Hdh150 mice exhibit anxiolytic behavior. (a) Representative travel pathways of WT (left) and presymptomatic Hdh150 (right) mice analyzed in a 5 min open field test. (b) Increased explorative behavior of Hdh150 animals compared to the WT mice. Mann-Whitney test, p<0.05.
DOI: https://doi.org/10.7554/eLife.38744.016

The following video, source data, and figure supplement are available for figure 3:

Source data 1. Numerical values of *Figure 3* and associated supplement figures.
DOI: https://doi.org/10.7554/eLife.38744.018

Figure supplement 1. Presymptomatic VFDO Hdh150 mice did not exhibit deficit in visual discrimination test and explorative behavior in novel object recognition test.
DOI: https://doi.org/10.7554/eLife.38744.017

Figure 3—video 1. Example of visual discrimination task performed by a trained mouse, real time.
DOI: https://doi.org/10.7554/eLife.38744.019

detected a clear reduction in the protein synthesis rate of a GFP-Htt fusion protein carrying 49 repeats in the metformin-treated samples in a concentration-dependent manner in primary neurons (*Figure 4c*, *Figure 4—source data 1*, RM two-way ANOVA p=0.008). This effect was confirmed in N2A cells (*Figure 4—figure supplement 1a*, *Figure 4—source data 1*, RM two-way ANOVA p=0.03). To further support the contribution of the MID1/PP2A/mTOR protein complex and PP2A activity to this effect, the GFP-Htt transfected cells were subsequently either (i) mock treated, (ii) treated with only metformin, (iii) treated with ocadaic acid (OA), or (iv) co-treated with metformin and OA. OA is an inhibitor of PP2A activity. As expected, OA significantly increased translation rates of the *GFP*-Htt reporter mRNA and metformin did not have a reducing effect on the translation rates in cells co-treated with OA suggesting that indeed the metformin effect is mediated by PP2A activity (*Figure 4d*, *Figure 4—source data 1*, RM two-way ANOVA p=0.002).

To analyze metformin effects on early signs of pathology *in vivo*, VFDO Hdh150 mice were fed with, or without 5 mg/ml metformin in the drinking water. Metformin did not significantly reduce drinking volume (*Figure 4—figure supplement 1b*, *Figure 4—source data 1*, RM two-way ANOVA not significant, see *Table 1* for p-values). After 3 weeks of treatment, we looked at phosphorylation patterns of the PP2A/mTOR target S6 and the amount of mHtt protein relative to wild-type Htt in whole brain tissue. The metformin-treated group showed a significant reduction of S6 phosphorylation suggesting an increase in PP2A activity (*Figure 4e and f*, *Figure 4—source data 1*, unpaired t-test p=0.05). At the same time, a slight tendency (not significant) of reduced mHtt was detected suggesting that metformin has an influence on mHtt expression (*Figure 4—figure supplement 1c and d*, *Figure 4—source data 1*, unpaired t-test not significant, see *Table 1* for p-values). A significant reduction of mHtt expression, however, became clearly visible after 11 weeks of treatment in cortical tissue (*Figure 4g–j*, *Figure 4—source data 1*, unpaired t-test, mHtt/wtHtt p=0.05, mHtt/Gapdh p=0.002, wtHtt/Gapdh p=0.9).
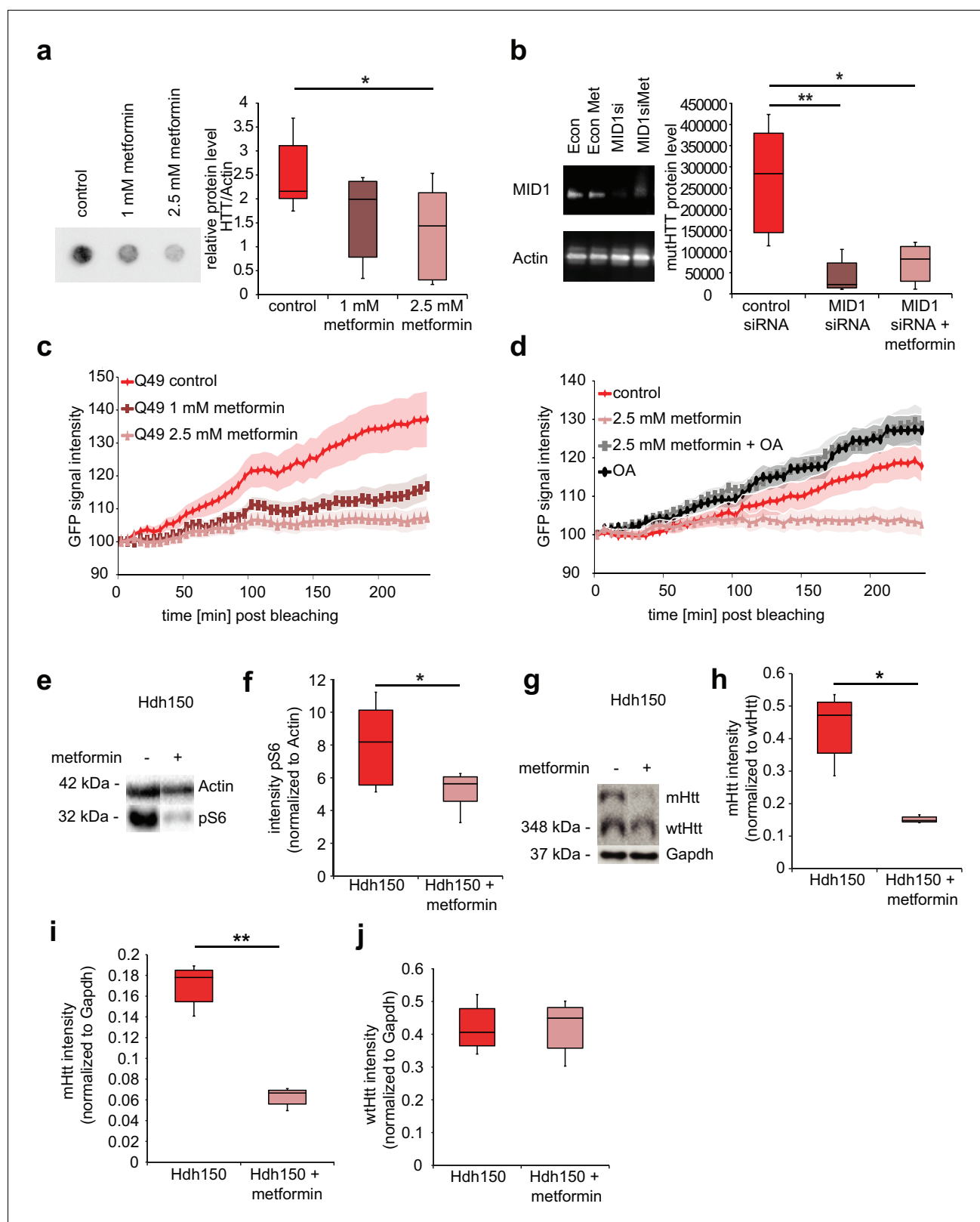
Figure 4. Metformin reduces translation rates of mutant HTT through MID1/PP2A protein complex *in vitro* and decreases both S6 phosphorylation and mutant Htt protein load in Hdh150 animals. (a) FLAG-HTT detected on a filter retardation assay after treatment with and without 1 mM and 2.5 mM metformin. Quantification on right panel. Mann-Whitney test, control vs. 1 mM metformin p=0.08; control vs. 2.5 mM metformin, p<0.05. (b) Stable cell line expressing FLAG-HTT exon1 with 83 CAG repeats transfected with *MID1*-specific siRNAs or control siRNAs in the presence or absence of 2.5 mM

Figure 4 continued on next page

Figure 4 continued

metformin. FLAG-HTT detected on a filter retardation assay. Efficiency of the knock-down including Actin as a loading control is shown on a western blot (left panel). Quantification of filter retardation assay on right panel. Mann-Whitney test, control siRNA vs. MID1 siRNA p<0.01; control siRNA vs. MID1 siRNA + metformin p<0.05. (c) Protein translation rate of GFP-tagged mutant Htt exon1 (49 CAG repeats) in primary cortical neurons measured in a FRAP-based assay, over a time frame of 4 hr. Lines show the GFP-signal intensity over time in mock-treated (control) and metformin-treated (1 mM and 2.5 mM) cells. Lines represent means, shadowed areas standard deviations. Repeated measures two-way ANOVA, treatment p<0.01, time p<0.0001; interaction p<0.0001. (d) Protein translation rate measured in a FRAP-based assay (see c). Lines show the GFP-signal intensity over time in mock-treated (control), metformin-treated (2.5 mM), ocadaic acid (OA)-treated and metformin +OA-treated cells. Shadowed areas show SEM. Repeated measures two-way ANOVA, treatment p<0.01, time p<0.0001, interaction p<0.0001. (e) Transgenic Hdh150 mice received metformin-containing water (5 mg/ml, Hdh150 +metformin) or pure water (Hdh150) over a period of 3 weeks. Whole brain lysates were analyzed for the phosphorylation of S6, the expression of total S6, mHtt and wtHtt on western blots. Representative western blots are shown. (f) Quantification of pS6 relative to S6. Unpaired t-test, p<0.05. (g) mHtt and wt Htt proteins of prefrontal cortex lysates analyzed on western blots after 11 weeks of treatment with metformin (5 mg/ml, Hdh150 +metformin) or pure water (Hdh150). Representative western blots are shown. (h) Quantification of mHtt relative to wtHtt. Treatment of 5 mg/ml metformin in the drinking water showed a significant reduction of mHtt protein compared to water control treatment. Unpaired t-test p <<0.05 (i) Quantification of mHtt relative to Gapdh. Unpaired t-test, p<0.01. (j) Quantification of wtHtt relative to Gapdh. Unpaired t-test, p=0.88.
DOI: https://doi.org/10.7554/eLife.38744.020

The following source data and figure supplements are available for figure 4:

Source data 1. Numerical values of *Figure 4* and associated supplement figures.
DOI: https://doi.org/10.7554/eLife.38744.023
Figure supplement 1. Metformin reduces mutant Htt protein translation and does not change drinking behavior of Hdh150CAG animals.
DOI: https://doi.org/10.7554/eLife.38744.021
Figure supplement 2. Metformin treatment rescues motility impairment in a *C.elegans* model.
DOI: https://doi.org/10.7554/eLife.38744.022

Metformin reverses signs of Huntington's disease pathology

Our data suggest metformin as a promising molecule to interfere with VFDO Huntington's disease biochemical and cellular pathological changes. We initially used a *C. elegans* model of polyQ-mediated diseases to test whether metformin effectively ameliorates disease symptoms in an easily controllable model with short lifespan. The *C. elegans* worms carry a transgene encoding YFP-tagged Q40 polypeptide in body wall muscle cells (*Morley et al., 2002*). Adult Q40::YFP nematodes exhibit intracellular aggregates of polyglutamine-containing protein and develop progressive paralysis over time, which is reflected in significantly reduced motility. We counted aggregates in metformin-treated and untreated nematodes. Moreover, we assessed their motility in a liquid thrashing experiment, in which worms are placed in liquid and the frequency of lateral swimming (thrashing) movement is analyzed as a measure of motility. We found that 5 days of metformin treatment reduced the number of intracellular inclusion bodies significantly and rescued motility impairment (*Figure 4—figure supplement 2a and b*, *Figure 4—source data 1*, Mann-Whitney, p<0.0001). Since bacteria can metabolize metformin (*Cabreiro et al., 2013*), we confirmed the results on heat-inactivated OP50 bacteria (*Figure 4—figure supplement 2c*, *Figure 4—source data 1*, Mann-Whitney test, control vs 5 mM metformin p=0.008, control vs 10 mM metformin p<0.0001). siRNA-mediated knock-down of arc-1, the *C.elegans* MID1 homolog, leads to a reduction of inclusion bodies and improved motility similar to the metformin effects (*Figure 4—figure supplement 2d and e*, *Figure 4—source data 1*, Mann-Whitney test, p<0.0001) and confirms that the MID1/PP2A/mTOR protein complex underlies metformin effects.

We then asked whether metformin could rescue the altered cortical activity *in vivo* in Hdh150 mice. Metformin treatment did not affect the density of OGB-1 stained cells (*Figure 5—figure supplement 1a,b*, *Figure 5—source data 1*, WT: 1413 ± 74 cells/mm^2 (n = 11 mice), Hdh150: 1456 ± 90 cells/mm^2 (n = 10 mice), WT met: 1351 ± 65 cells/mm^2 (n = 9 mice) and Hdh150 met: 1448 ± 60 cells/mm^2 (n = 6 mice), unpaired t-test, not significant, see *Table 1* for p-values). Notably, 3 weeks of metformin treatment in the drinking water completely restored the proportion of active cells (*Figure 5b*, *Figure 5—source data 1*, Hdh150: $77.2 \pm 3.5\%$ (n = 6 mice), Hdh150 met: $64.4 \pm 4.1\%$ (n = 6 mice), Mann-Whitney test p<0.05) and the average frequency of Ca^{2+} transients (*Figure 5a,c*, *Figure 5—source data 1*, Hdh150: 1.2 ± 0.1 trans/min (n = 6 mice), Hdh150 met: $0.7 \pm 0.06\%$ (n = 6 mice), Mann-Whitney test p<0.05). The individual traces of treated Hdh150 animals were indistinguishable from untreated WT animals (*Figure 5a*, *Figure 5—figure supplement 1c*).
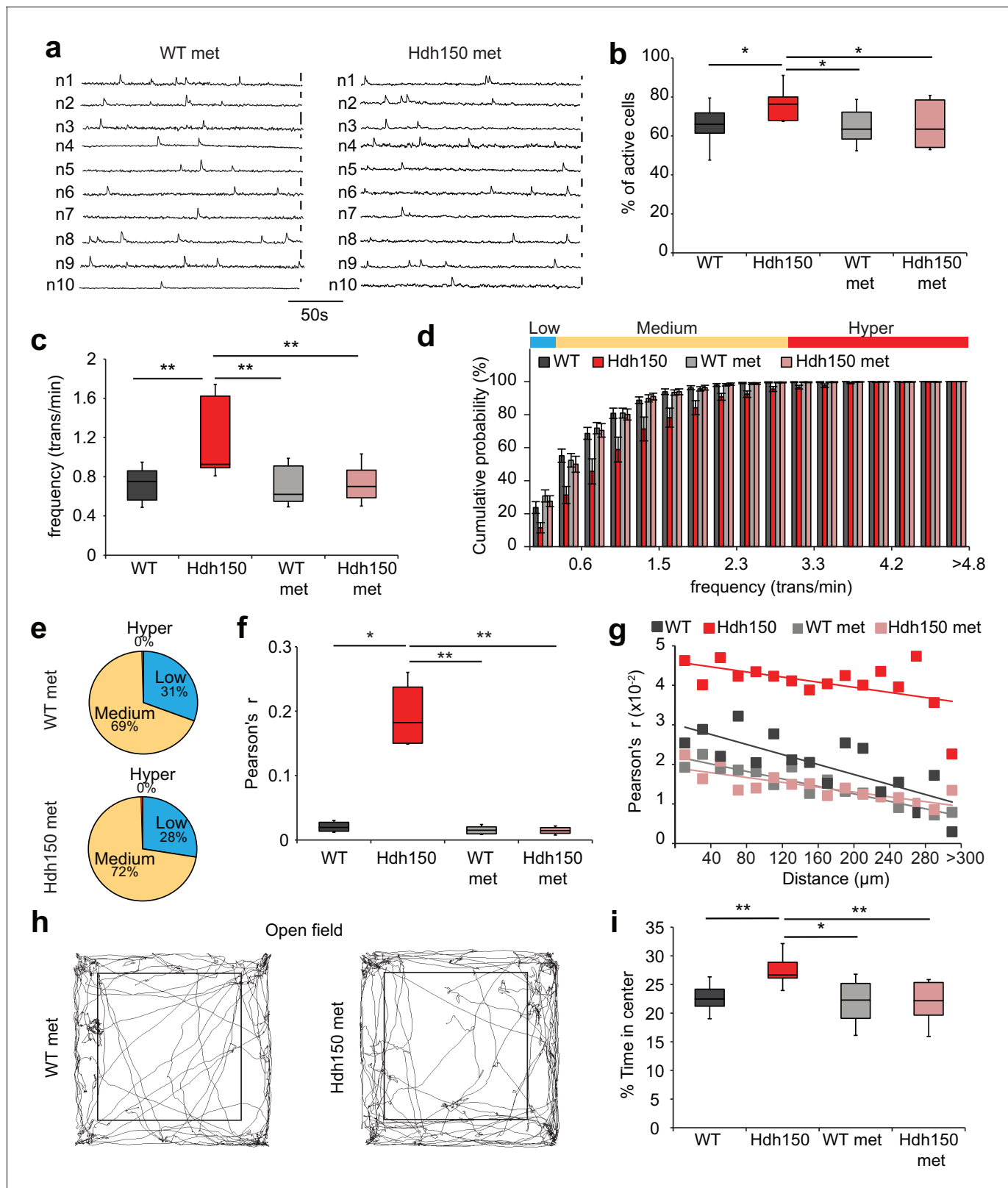
Figure 5. Metformin treatment reverses pathological neuronal network activity and behavioral abnormalities in presymptomatic VFDO Hdh150 mice. (a) Representative traces of spontaneous Ca^{2+} transients of 10 neurons recorded *in vivo* in WT and Hdh150 mice after metformin treatment. Vertical scale bar: 40% dF/F. (b) Relative proportion of spontaneously active neurons in WT (dark grey), Hdh150 (red), WT metformin-treated (light grey) and Hdh150 metformin-treated (light red) mice. Mann-Whitney test, WT vs. Hdh150, p<0.05; Hdh150 vs. Hdh150 met, p<0.05; Hdh150 vs. WT met, p<0.05.
Figure 5 continued on next page

Figure 5 continued

(c) Significant reduction in the spontaneous Ca^{2+} transient frequency to WT levels in Hdh150 mice after metformin treatment (red vs. light red). Mann-Whitney test, WT vs. Hdh150, p<0.01; Hdh150 vs. Hdh150 met, p<0.01; Hdh150 vs. WT met, p<0.01. (d) Cumulative frequency distributions of Ca^{2+} transients in WT (dark grey), Hdh150 (red), metformin-treated WT (light grey) and metformin-treated Hdh150 (light red) mice. Top, color-coding of active neurons by frequency. Two-way ANOVA test, Group: p<0.0001; Time: p<0.0001; Interaction: p<0.0001. (e) Pie charts showing the relative proportion of low (blue), medium (orange) and hyperactive (red) neurons in layer 2/3 of the visual cortex in WT (top) and Hdh150 (bottom) mice after metformin treatment. Chi-square test, p=0.62, Chi-square = 0.24. (f) Comparison of Pearson's r between a pair of neurons in WT (dark grey), Hdh150 (red), metformin-treated WT (light grey) and metformin-treated Hdh150 (light red) mice. Mann-Whitney test, WT vs. Hdh150, p<0.05, Hdh150 vs. Hdh150 met, p<0.01, Hdh150 vs. WT met, p<0.01. (g) Relationship between pairwise Pearson's r and pairwise distance in metformin-treated WT (light grey) and Hdh150 (light red) mice. Two-way ANOVA test, group p<0.0001; Distance p=0.09; Interaction p<0.001. (h) Representative travel pathways of a metformin-treated WT (left) and pre-symptomatic Hdh150 (right) mice analyzed in a 5 min open-field test. (i) Decrease in the explorative behavior of metformin-treated Hdh150 animals. Mann-Whitney test, WT vs. Hdh150, p<0.01; Hdh150 vs. Hdh150 met, p<0.001; Hdh150 vs. WT met, p<0.05; WT vs. Hdh150 met, p=0.8.

DOI: https://doi.org/10.7554/eLife.38744.024

The following source data and figure supplement are available for figure 5:

Source data 1. Numerical values of *Figure 5* and associated supplement figures.

DOI: https://doi.org/10.7554/eLife.38744.026

Figure supplement 1. Metformin treatment does not affect cell density or Ca^{2+} transient dynamics

DOI: https://doi.org/10.7554/eLife.38744.025

Importantly, in these experiments, metformin acts specific on dysregulated network components. Only the AUC of calcium transients was slightly yet significantly affected in WT mice which might be due to an increase of baseline calcium concentration induced by the activation of MID1/PP2A/mTOR signaling pathway (*Figure 5—figure supplement 1c*, *Figure 5—source data 1*). One of the hallmarks of the VFDO Hdh150 mice was the distinct functional subgroup of hyperactive neurons (*Figure 1*). We thus assessed the effect of metformin treatment on the relative proportions of low, normal and hyperactive subgroups. Treatment with metformin in Hdh150 mice led to the complete abolishment of the hyperactive subgroup (*Figure 5d*, *Figure 5—source data 1*, two-way ANOVA p<0.0001 and *Figure 5e*, *Figure 5—source data 1*, Chi-square test not significant, see *Table 1* for p-values) and restored the relative proportion of functional subgroups. The spatial distribution of functional subgroups remained unchanged by metformin treatment (*Figure 5—figure supplement 1f*, *Figure 5—source data 1*, Mann-Whitney test, not significant, see *Table 1* for p-values). This complete restoration of dysregulated microcircuit activity was also evident in the cumulative frequency distribution (*Figure 5d*, *Figure 5—source data 1*) and all other network measures found to be aberrant in young Hdh150 animals, such as synchronicity (*Figure 5f and g*, *Figure 5—figure supplement 1d–e*, *Figure 5—source data 1*).

Accompanying the network dysfunction, we observed anxiolytic behavior in the VFDO Hdh150 mice (see *Figure 3a–b*). Treatment with metformin fully reversed the anxiolytic behavior (*Figure 5h and i*, *Figure 5—source data 1*, Mann-Whitney test, WT vs Hdh150 p=0.002, Hdh150 vs Hdh150 met p=0.002, Hdh150 vs WT met p=0.03, WT vs Hdh150 met p=0.8).

In conclusion, our data suggest that metformin, by interfering with the translation rate of mHtt protein, reduces protein load in cell culture and *in vivo* and reverses early Huntington's disease-related network dysregulations as well as anxiety-related behavioral aberrations in mice. Furthermore, usage of metformin in adult *C. elegans,* a model of polyQ disease, also significantly influences inclusion bodies formation and motility.

Discussion

Here, we have identified a dysregulation of spontaneous neuronal activity in the visual cortex in a very early stage of a mouse model of Huntington's disease that corresponds to a very early stage in the premanifest stage in Huntington's disease mutation carriers (*Figure 1a,b*), which might indeed be a distinct pathological disease stage which is very far from disease onset (VFDO). Correspondingly, the visual cortex is one of the first structures affected in patients (*Labuschagne et al., 2016*; *Dogan et al., 2013*). This dysregulation is characterized by an

increase in cortical network activity patterns, the emergence of a functional subgroup of hyperactive neurons, and enhanced synchronicity. Overall visual cortex functioning seems to be preserved at this early time point of Huntington's disease course. Network changes are accompanied by subtle behavior alterations including an anxiolytic phenotype, suggesting that at least part of the brain-wide circuitry exhausted its compensational reserve. Anxiety-related abnormalities including anxiolytic behavior have previously been described in the preclinical phase in several other rodent Huntington's disease models ((*Nguyen et al., 2006*), reviewed in [*Pouladi et al., 2013*]). So far, changes described here represent the earliest identified abnormalities in cortical pathophysiology and behavior in heterozygous Hdh150 animals, which closely resemble the human disease (*Lin et al., 2001*; *Heng et al., 2007*; *Brooks et al., 2012*; *Tallaksen-Greene et al., 2005*). Furthermore, we show that the type II diabetes drug metformin inhibits the translation of mHtt protein and thereby decreases mHtt protein load *in vitro* and *in vivo*. Promisingly, this leads to a complete restoration of VFDO network activity patterns as well as behavior abnormalities under chronic metformin therapy.

Our data report primal changes in cortical network function in the VFDO stage of Huntington's disease. A recognition of the network as a pathophysiological entity has recently been suggested in the context of Alzheimer's disease (*Busche et al., 2008*; *Iaccarino et al., 2016*). Moreover, focus has shifted away from the mechanisms accompanying neuronal and network degeneration and instead moved toward small and subtle functional changes at very early stages of the disease when irrevocable damage to the network has not yet occurred (*Busche and Konnerth, 2016*). Indeed, hyperactive neurons are associated with both advanced and early stages of Alzheimer's disease, independent of plaque formation (*Busche et al., 2012*; *Busche et al., 2008*). In addition, evidence points toward hyperactive neurons preventing the cortex-wide propagation of slow oscillations in early Alzheimer's disease (*Busche et al., 2015*).

We here describe a similarly distinct hyperactive phenotype in very early stages of Huntington's disease. We conclude that neuronal hyperactivity may be a principle mechanism that develops early not only in Alzheimer's disease but also in other neurodegenerative diseases. Thus, the notion of early network dysregulation as a therapeutic target may have broad implications.

Similar to early stages of Alzheimer's disease hyperactive neurons in Hdh150 animals emerge in the absence of aggregate formation. Also hyperactive cells do not cluster, and reactive astrocytes or cells with activated caspase-3 as a marker of early apoptosis are not found in these early stages of Huntington's disease. Furthermore, cortical neurons did not exhibit metabolic dysregulation as measured in a mitochondrial respiration assay. Therefore, we may postulate that the cortex merely responds to early pathophysiological events already commencing in subcortical regions, e.g. the striatum. This is well in line with the current emerging hypotheses of disease progression in Alzheimer's disease. Young Alzheimer's disease animals develop hyperactivity in a plaque-independent fashion first in the hippocampus (possibly due to higher vulnerability of the hippocampus in Alzheimer's disease), followed by a similar hyperactivity pattern in the cortex later in the disease process (*Busche et al., 2012*; *Busche et al., 2008*). Furthermore, in Alzheimer's disease patients, degeneration of cortical projection targets of the hippocampus is associated with hippocampal hyperactivity indicating a connectivity-based spread of network dysregulations eventually leading to neurodegeneration (*Putcha et al., 2011*). Our data indeed suggest an altered activity in subcortical drivers, since unspecific alteration of excitability in individual neurons is unlikely to lead to an increase in synchronicity, but rather would result in a random increase in firing.

Our data was collected at very early stages of the disease in the Hdh150 mouse model, which corresponds to the VFDO stage in Huntington's disease patients. The importance of expression of mutant Htt protein during very early phases for disease development has been demonstrated in the BACHD:CAG-Cre^ERT2 mouse (*Molero et al., 2016*). With the help of tamoxifen treatment expression of mutant Htt was turned off early postnatally. Still the typical symptoms of Huntington's disease at three and nine months of age were observed in the animals. We conclude that only at the VFDO stages, when cellular and network degeneration have not yet been established, preventive strategies will be most effective; only then can we still rescue small homeostatic shifts, prevent spreading and potentially stabilize network function.

Phenotype reversal could be demonstrated in a tetracyclin-dependent conditional mouse model for Huntington's disease. Both neuropathological findings and behavior aberrations were found to disappear when mHtt protein production was stopped through a tet-off regulation mechanism in the

adult animal (*Yamamoto et al., 2000*). Additional support for the beneficial effect of suppression of aberrant protein production on the Huntington's disease phenotype stems from several studies with RNA interference (siRNA), or antisense oligonucleotides showing that gene suppression reducing mHtt protein load by 40% or more, is sufficient to significantly ameliorate the Huntington's disease phenotype (*HD iPSC Consortium, 2017*; *Harper et al., 2005*; *Keiser et al., 2016*; *Stanek et al., 2014*). These studies have demonstrated, that (i) the earlier suppression takes place the more robust and beneficial effects on behavior phenotypes are [reviewed in (*Keiser et al., 2016*)] and (ii) that even transient suppression of Htt protein during early disease stages was sufficient to obtain long-term effects on the disease phenotype lasting for months, far beyond the treatment period (*Lu and Yang, 2012*; *Kordasiewicz et al., 2012*).

However, developing siRNA and antisense oligonucleotides technologies into therapeutics for clinical use is difficult and a long way to go. Difficulties here include toxicity and modes of delivery: so far oligonucleotides have to be regularly injected into the cerebrospinal fluid, which is a huge effort for patients and physicians. Furthermore, a short N-terminal fragment of the mHtt protein, mHttexp1p, that is produced by incomplete exon one splicing and a short poly-adenylated mRNA in several animal models as well as in Huntington's disease patients rather than full-length mHtt protein was found to be particularly pathogenic. Its occurrence correlates well with age of onset and severity of the disease. This short mRNA is difficult to target by oligonucleotide strategies (*Neueder et al., 2017*; *Sathasivam et al., 2013*). We show here that a well-known, widely used, orally delivered small compound, metformin, suppresses mHtt production by targeting both, full-length and mHttex1p, *in vitro* and *in vivo* and thereby significantly reduces mHtt protein load, which makes it a very promising candidate for chronic early onset Huntington's disease therapy.

Metformin is an FDA-approved, inexpensive biguanide that has been used in patients with Type II diabetes for decades and is under discussion for cancer preventive therapy (*Demir et al., 2014*; *Micic et al., 2011*). Very recently, metformin has been shown to rescue core phenotypic features in a mouse model for fragile X-syndrome, a neurodevelopmental disorder, by normalizing ERK signalling (*Gantois et al., 2017*).

Metformin had been brought in as a promising compound in Huntington's disease previously. It has been found to protect cells from the toxicity of mutant Huntingtin protein in a cell culture model (*Jin et al., 2016*). In a study on R6/2 animals, a very aggressive model for Huntington's disease, Ma and colleagues had found a significant effect on survival rates and hind clasping in male animals only when given metformin in the drinking water starting from week 5 (*Ma et al., 2007*). In relation to the phenotype in the R6/2 animals that develops severe aberrations from 4 weeks on this is a late time point and would be placed in the motor phase stage when projected to the phenotypic time line given in *Figure 1a*. We hypothesize here that preventive treatment at a very early stage is important to substantially and stably influence the disease. This is in agreement with observations in a mouse model for spinocerebellar ataxia I, another neurodegenerative disease based on CAG expansion and studies with antisense oligonucleotides in a Huntington's disease model. Both studies show that gene suppression has more stable effects on the phenotype when performed early enough (*Kordasiewicz et al., 2012*; *Rubinsztein and Orr, 2016*; *Zu et al., 2004*). In line with that only two phenotypic features had been found to react on late metformin treatment- survival rates and frequency of clasping- in the R6/2 animals. Also and again as expected, effect size on animal survival was quite small (p=0.02). Gender differences in response rate seen in this study can possibly be explained by gender differences in disease development and progression at the motor stage, which had been observed in several mouse models (*Menalled et al., 2009*). When disease progression differs, differences in blood brain barrier permeability can be expected (reviewed in [*Sweeney et al., 2018*]) which then is likely to lead to gender specific variation in bioavailability of metformin in the brain. In contrast to this study we here show that *in vivo* metformin has highly significant effects (p=0.03 to p<0.0001) already on primal changes in the very early, VFDO phases of Huntington's disease making metformin a promising compound for the development of a therapeutic scheme that is based on early prevention of pathology development. While we focused on male mice in this study, to reduce physiological variability due to hormone fluctuations, at the VFDO stage brain barrier changes are not expected to influence bioavailability of metformin.

Metformin was suggested to lead, through AMPK activation, to a reduction of mHtt aggregates *in vitro* (*Walter et al., 2016*; *Vázquez-Manrique et al., 2016*). In our previous work, however, we

have shown that in cortical neurons metformin does not induce phosphorylation of the AMPK target ACC at all and only when given chronically it induces phosphorylation of AMPK itself in vitro. When giving 5 mg/ml metformin in the drinking water for 16 – 24 days to wildtype animals, while phosphorylation of S6 is significantly reduced, AMPK phosphorylation does not change in whole brain extracts (*Kickstein et al., 2010*). This indicates that AMPK activation is likely to depend on the dose. In WT animals as in preclinical Huntington's disease animals the blood-brain barrier is intact, which limits bioavailability of metformin in the brain. Metformin concentrations needed to influence mTOR/PP2A activity seem to be significantly lower than those needed to influence AMPK activity. Like in the Kickstein et al. paper, in the present study, we used 5 mg/ml metformin in the drinking water, a concentration at which AMPK activation is not expected, but as we show here in the Hdh150 animals, metformin has a significant effect on the phosphorylation of the mTOR/PP2A target S6.

The effect of Htt loss on brain function is still under debate. SiRNA studies suggest that postnatal reduction of endogenous Htt protein is well tolerated (summarized in [*Keiser et al., 2016*]). However, conditional knock-out animals with a perinatal loss of around 40% of Htt protein in the forebrain show a neurodegenerative phenotype (*Dragatsis et al., 2000*). Likewise, depletion of Htt protein in the adult brain leads to progressive behavior deficits (*Dietrich et al., 2017*). We demonstrate here that metformin has a very specific effect on the expression of mHtt protein only, leaving wild-type Htt that is produced from the non-mutated allele in dominant Huntington's disease untouched (*Figure 4*). This makes metformin the only compound available at present with a specific effect on only mutant but not wild-type Htt protein.

In support of an effect of metformin in Huntington's disease patients an *in silico* comparison of cognitive performance of Huntington's disease patients treated with metformin was performed. In this study, using the Enroll patient cohort, it was shown that diabetic Huntington's disease patients in the manifest stage treated with metformin had a better cognitive performance than Huntington's disease patients not treated with metformin (*Hervás et al., 2017*).

Our data indicate that metformin treatment reverses all cortical network dysregulations *in vivo* in the premanifest VFDO Hdh150 mice including functional sub-group distribution, frequency and synchronicity. Regaining network stability shows promise for ameliorating the molecular pathophysiology, probably by activating intrinsic repair mechanisms as shown in the context of Alzheimer's disease (*Iaccarino et al., 2016*; *Keskin et al., 2017*). Following this network-centered view, restoration of network functions might also prevent secondary damage to the neuronal microcircuit. We therefore propose a shift in experimental treatment strategies: rather than exploring single pathways for target, we might also consider re-balancing network function in the VFDO stages of the disease.

Taken together, our data provide evidence for the existence of a pathophysiological entity very far from onset of the manifest disease (VFDO) characterized by early homeostatic changes of network activity and, associated with that, subtle behavior alterations. The data also strongly support the observation that, similar to humans, the disease in mice develops over a long period of time. This provides an early critical window of vulnerability and gives opportunities for early therapeutic interference with disease development. So far, all attempts to develop a causative therapy for Huntington's disease have been unsuccessful [summarized in (*Crook and Housman, 2011*; *Clabough, 2013*)]. In terms of therapeutic intervention, consideration should be given to a chronic treatment of mutation carriers, which covers the critical windows of vulnerability, as early as in the VFDO stages. Such a strategy avoids delaying intervention until clinical signs of the disease are evident, implying that substantial brain damage has already occurred. Our data suggest that metformin has the potential to reduce mHtt protein load and to substantially influence the early development of pathology and, as seen in a *C. elegans* model, protein aggregation and movement aberrations which are pathognomonic for later disease stages. It is an inexpensive substance, well known in long-term clinical usage and has a defined, relatively benign spectrum of side effects. Prescription to mutation carriers from young adulthood on (or even earlier) is possible and will cover these newly discovered critical windows of opportunity for therapy.

Materials and methods

Key resources table

Reagent type (species) or resource	Designation	Source or reference	Identifiers	Additional information
Genetic reagent (*C.elegans*)	*C.elegans* strain AM141, genotype rmls133	University of Minnesota	AM141 (WormBase ID) RRID:WB-STRAIN:AM141	
Genetic reagent (*M. Musculus*)	Hdh150	Jackson Laboratory	#004595 RRID:IMSR_JAX:004595	Only males were used
Cell line (*H. sapiens*)	HEK 293T/17	*Scherzinger et al. (1997)*	CRL-11268 RRID:CVCL_1926	
Cell line (*M. Musculus*)	Neuro-2A	ATCC	ATCC CCL131 RRID:CVCL_0470	
Cell line (*M. Musculus*)	primary cortical neurons	isolated from NMRI (Janvier)		
Transfected construct	pEGFP-C1-Httex1	*Krauss et al., 2013*	Self-cloned	
Antibody	rabbit anti-activated-caspase-3	Cell signaling	9661 RRID:AB_2341188	1 to 500
Antibody	mouse anti-NeuN	Millipore	MAB377 RRID:AB_2298772	1 to 500
Antibody	rabbit anti-GFAP	Dako	Z0334 RRID:AB_10013382	1 to 1500
Antibody	rabbit anti-Htt	Abcam	ab109115 RRID:AB_10863082	WB: 1:850, IHC: 1:200
Antibody	Alexa 546 goat anti-rabbit	Invitrogen	A11035 RRID:AB_143051	1 to 300
Antibody	Alexa 647 goat anti-mouse	Invitrogen	A21235 RRID:AB_141693	1 to 300
Antibody	Cy2 donkey anti-rabbit	Jackson Immuno Research	711-225-152 RRID:AB_2340612	1 to 300
Antibody	Alexa 488 goat anti-rabbit	Life technologies	A11008 RRID:AB_143165	1 to 200
Antibody	anti-FLAG M2-Peroxidase	Sigma-Aldrich	A8592 RRID:AB_439702	1 to 3000
Antibody	rabbit anti-actin	Sigma-Aldrich	A2066 RRID:AB_476693	1 to 2000
Antibody	rabbit anti-pS6	Cell signaling	2215 RRID:AB_2630325	1 to 2000
Antibody	mouse anti-GAPDH	Abcam	ab8245 RRID:AB_2107448	1 to 2000
Antibody	HRP-anti-mouse	Dianova	115-035-072 RRID:AB_2338507	1 to 6000
Antibody	HRP-anti-rabbit	Dianova	305-036-003 RRID:AB_2337936	1 to 6000
Antibody	goat anti-rabbit IgG, AlexaFluor 488 conjugate	Life technologies	A11008 RRID:AB_143165	1 to 200
Sequence-based reagent	primers 5'-CCC ATT CAT TGC CTT GCT GCT AGG-3' and 5'-CCT CTG GAC AGG GAA CAG	Sigma-Aldrich	custom	
Sequence-based reagent	siRNA AATTGACAGAG GAGTGTGATC	Qiagen	custom	
Sequence-based reagent	siRNA CACCGCAUCCUAGUAUCACACTT	Qiagen	custom	

Continued on next page

Continued

Reagent type (species) or resource	Designation	Source or reference	Identifiers	Additional information
Sequence-based reagent	siRNA CAGGAUUACAACUUUUAGGAATT	Qiagen	custom	
Sequence-based reagent	siRNA TTGAGTGAG CGCTATGACAAA	Qiagen	custom	
Sequence-based reagent	siRNA AAGGTGAT GAGGCTTCGCAAA	Qiagen	custom	
Sequence-based reagent	siRNA TAGAACGT GATGAGTCATCAT	Qiagen	custom	
Sequence-based reagent	non siRNA AATTCTCCG AACGTGTCACGT	Qiagen	custom	
Chemical compound, drug	Hoechst33342	Sigma-Aldrich	B2261 CHEBI:51232	1 to 1000
Chemical compound, drug	Fluoromount	Sigma-Aldrich	F4680	
Chemical compound, drug	Fluoroshield Mounting Medium	Abcam	ab104135	
Chemical compound, drug	PBS tabletts	gibco	18912–014	
Chemical compound, drug	Triton-X	Roth	6683.1 CHEBI:9750	0.3%
Chemical compound, drug	Tween20	Roth	9127.1	0.1%
Chemical compound, drug	Triton X-100	Sigma-Aldrich	T8787 CHEBI:9750	1 – 0.1%
Chemical compound, drug	natural donkey serum	Abcam	ab7475 RRID: AB_2337258	4 – 2%
Chemical compound, drug	natural goat serum	Abcam	ab7481 RRID:2532945	4 – 2%
Chemical compound, drug	natural sheep serum	Abcam	ab7489 RRID: AB_2335034	20%
Chemical compound, drug	xylocaine	AstraZeneca	PUN080440	2%
Chemical compound, drug	isoflurane	AbbVie	8506 CHEBI:6015	1–1.55%
Chemical compound, drug	PBS	Life technologies	18912–014	1 M
Chemical compound, drug	paraformaldehyde	Life technologies	15710 CHEBI:31962	diluted to 4%
Chemical compound, drug	Oregon-Green BAPTA1 AM	Molecular probes	O6807	1 mM
Chemical compound, drug	EGTA	Sigma-Aldrich	E4378 CHEBI:30740	0.5 mM
Chemical compound, drug	MgCl2	Sigma-Aldrich	M2670 CHEBI:86345	3 mM
Chemical compound, drug	K-lactobionate	Sigma-Aldrich	L2398 CHEBI:55481	60 mM
Chemical compound, drug	Taurine	Sigma-Aldrich	T0625 CHEBI:15891	20 mM
Chemical compound, drug	KH_2PO_4	Sigma-Aldrich	P5655 CHEBI:63036	10 mM
Chemical compound, drug	HEPES	Sigma-Aldrich	H3375 CHEBI:42334	20 mM

Continued on next page

Continued

Reagent type (species) or resource	Designation	Source or reference	Identifiers	Additional information
Chemical compound, drug	Sucrose	Sigma-Aldrich	S0389 CHEBI:17992	110 mM
Chemical compound, drug	BSA	Sigma-Aldrich	A6003	1 g/L
Chemical compound, drug	Malate	Sigma-Aldrich	M1000 CHEBI:6650	2 mM
Chemical compound, drug	Pyruvate	Sigma-Aldrich	P2256 CHEBI: 50144	10 mM
Chemical compound, drug	Glutamate	Sigma-Aldrich	G1626 CHEBI:64243	20 mM
Chemical compound, drug	ADP	Sigma-Aldrich	A2754 CHEBI:16761	5 mM
Chemical compound, drug	Succinate	Sigma-Aldrich	S2378 CHEBI:63686	10 mM
Chemical compound, drug	FCCP	Sigma-Aldrich	C2920 CHEBI:75458	0.2 μM
Chemical compound, drug	Rotenone	Sigma-Aldrich	R8875 CHEBI:28201	0.1 μM
Chemical compound, drug	Antimycin A	Sigma-Aldrich	A8674 CHEBI:22584	2 μM
Chemical compound, drug	$MgSO_4$	Sigma-Aldrich	203726 CHEBI:32599	
Chemical compound, drug	NaCl	Sigma-Aldrich	S3014 CHEBI:26710	
Chemical compound, drug	Na_2HPO_4	Sigma-Aldrich	S3264 CHEBI:34683	
Chemical compound, drug	oligofectamine	Thermo-Fisher	12252–011	0.2%
Chemical compound, drug	metformin	MP Biomedicals	157805 CHEBI:6802	5 mg/ml
Chemical compound, drug	urea	Roth	2317.3 CHEBI:16199	48%
Chemical compound, drug	Tris	Roth	4855.2 CHEBI:9754	15 mM
Chemical compound, drug	Glycerin	Roth	3783.1 CHEBI:17754	8.7%
Chemical compound, drug	SDS	Roth	2326.1 CHEBI:8984	1%
Chemical compound, drug	mercaptoehanol	Roth	4227.3 CHEBI:41218	1%
Chemical compound, drug	protease inhibitors	Roche	04 693 116 001	1 tablet per 50 ml
Chemical compound, drug	Phosstop	Roche	04 906 837 001	2 tablets per 10 ml
Software, algorithm	GraphPad Prism	GraphPad Prism	RRID:SCR_002798	http://www.graphpad.com/
Software, algorithm	Igor Pro 6.22 – 6.37	Wavemetrics	RRID:SCR_000325	http://www.wavemetrics.com/products/igorpro/igorpro.htm
Software, algorithm	MATLAB R2011a	Mathworks	RRID:SCR_001622	https://www.mathworks.com

Continued on next page

Continued

Reagent type (species) or resource	Designation	Source or reference	Identifiers	Additional information
Software, algorithm	Code use for Calcium transient analysis	this paper		the code is enclosed as a source file
Software, algorithm	LaVision BioTec ImSpector microscopy software	LaVision BioTec	RRID:SCR_015249	https://www.lavisionbiotec.com/
Software, algorithm	Fiji	Fiji	RRID:SCR_002285	http://fiji.sc
Software, algorithm	Image J	Image J - NIH	RRID:SCR_003070	https://imagej.nih.gov/ij/
Software, algorithm	EthoVision XT 8.5	Noldus	RRID:SCR_000441	https://www.noldus.com/EthoVision-XT/New
Software, algorithm	Image lab	Biorad	RRID:SCR_014210	http://www.bio-rad.com/en-us/sku/1709690-image-lab-software
Software, algorithm	Oroboros DatLab	Oroboros, Innsbruck, Austria		http://www.oroboros.at/index.php?id=datlab

Animals

All experimental procedures were performed in accordance with institutional animal welfare guidelines and were approved by the state government of Rhineland-Palatinate, Germany (G14-1-010 and G14-1-017). WT littermates and heterozygous $Hdh^{(CAG)150}$ mice (Hdh150, RRID:IMSR_JAX:004595) carrying an extended CAG sequence (~150) replacing the normal length CAG sequence in mouse *Htt* gene were obtained by crossing Hdh150 heterozygous with WT mice (*Lin et al., 2001*).

Male mice at 10 – 15 weeks of age were used to examine the change in neuronal network activity prior to disease onset and at 14 – 17 weeks of age to examine the effect of *in vivo* metformin treatment. Male mice at 12 – 16 weeks of age were used for behavior studies. Male mice at 13 weeks of age were used for immunohistochemistry. The mice were kept under specific-pathogen-free conditions on a 12 hr light/12 hr darkness cycle with free access to water and food. Mice were genotyped using the primers 5'-CCC ATT CAT TGC CTT GCT GCT AGG-3' and 5'-CCT CTG GAC AGG GAA CAG TGT TGG-3' (Sigma-Aldrich) producing 379- and 829-bp-long fragments for WT and mutant alleles, respectively.

Surgery for *in vivo* two-photon Ca^{2+} imaging

Mice were prepared for *in vivo* imaging under isoflurane (1 – 1.5% in pure O$_2$, AbbVie). Anesthesia depth was assessed by monitoring pinch withdrawal and respiration rate. Body temperature was kept at 37°C with a heating pad (ATC 200, World precision instruments). Local anesthesia (2% xylocaine, AstraZeneca) was applied to the scalp. A custom-made recording chamber was glued to the skull with cyanoacrylic glue (UHU) followed by dental cement (Paladur, Heraeus). Then, a craniotomy of 1.5 × 1.5 mm was performed using stainless steel drill bits. The position of the primary visual cortex was located according to brain atlas coordinates (Bregma −3 to −4.5 mm, 2 – 3 mm lateral to the midline) (*Paxinos and Franklin, 2001*). After surgery, the mouse was subjected to the two-photon imaging setup.

Two-photon Ca^{2+} imaging

The fluorescent Oregon-Green BAPTA1 AM (OGB-1 AM, O6807, Molecular Probes) was bulked-loaded in the visual cortex as described previously (*Stosiek et al., 2003*). Anesthesia level was continuously monitored by keeping the breathing rate at 100 – 110 breaths/min. High-speed two-

photon Ca^{2+} imaging was performed in layer 2/3 (150 to 350 μm from the pial surface) with an upright LaVision BioTec TrimScope II resonant scanning microscope, equipped with a Ti:sapphire excitation laser (Chameleon Ultra II, Coherent) and a 25x (1.1 N.A., MRD77220, Nikon) or 40x (0.8 N.A., NIRAPO, Nikon) objective. The laser was tuned to 800 nm and fluorescence emission was isolated using a band-pass filter (525/50, Semrock) and detected using a GaAsP photomultiplier tube (PMT; H7422-40, Hamamatsu). The TriM Scope II scan head, equipped with a resonant scanner, imaged time-lapses (512 × 512 pixels,~440 × 440 μm field of view) at a maximum frame rate of 30.4 Hz. Time lapses were recorded for 5 – 8 min on average. Imspector software (LaVision BioTec) was used for microscope control and image acquisition.

Determining cell number and analysis of Ca^{2+} transients

First, the number of cells loaded with OGB-1 was manually counted in ImageJ (National Institutes of Health). The area containing all the cells was traced freehand and calculated by the software. Functional data were analyzed using custom-written functions in MATLAB R2011a (Mathworks, Natick, MA) and Igor Pro 6.22 – 6.37 (Wavemetrics, Inc., Lake Oswego, OR). The code is attached as *Figure 1—source data 2*. Regions of interest (ROIs) were hand-drawn by tracing the outlines of OGB1-positive neurons. Fluorescence intensities were quantified by averaging pixels inside each ROI for every image in a sequence. The fluorescence values were normalized by user-defined baseline. Specifically, dF/F was defined as the following:

$$\frac{dF}{F} = \left(\frac{mean\ fluorescence\ inside\ an\ ROI}{mean\ user-defined\ baseline} - 1 \right) * 100$$

where the baseline is defined as a mean fluorescence from a 1–3 s silent period in the same ROI. The peak of a Ca^{2+} transient was defined as the first derivative to crossed zero, and the second derivative to be negative, and where the amplitude to be greater than three standard deviations (SD) above the mean. The peak location was corrected manually where necessary. Each dF/F trace, sampled at 15.2 – 30.4 Hz sampling frequency, was preprocessed by binomial Gaussian smoothing (20 – 40 iterations) followed by a high pass filter. The baseline was estimated as the median of activity-free 10 s period preceding each peak. The foot and the tail of Ca^{2+} transients were determined as the first data point that fell within 0.5 SD of the baseline before and after the peak, respectively. The area under the curve was trapezoidal and measured between the foot and the tail. A distribution histogram of neurons according to their Ca^{2+} transient frequency was used to segregate neurons into three functional subgroups. The definition of hyperactive neurons (>3 trans/min) was determined by the absence of neurons above this limit in WT (0.4 ± 0.3%). The criterion used for low active neurons was set to comprise ~25% of the WT neuronal population (25.8 ± 3.9%).

The distance between two neurons was calculated by Pythagorean theorem after the x,y coordinate was determined for each ROI.

The randomization of experimental data comprised two steps: first, each raster plot was reassigned to a randomly selected ROI; then, the location of the individual raster event was shuffled randomly, except no spikes were allowed to occur within 1 s of each other.

Immunohistochemistry

Mice were anesthetized with a mixture of ketamine/xylocaine and perfused transcardially with 4% paraformaldehyde (#15710, Life technologies) in 0.1M phosphate buffer and brains were post-fixed. 50-μm-thick sections were sliced using a HM650 V vibratome (ThermoFisher) and collected in phosphate buffer saline (PBS; Life technologies). Floating sections were incubated for 1 hr with PBS containing 4% natural goat serum (NGS, ab7481, Abcam) or 4% natural donkey serum (NDS, ab7475, Abcam) and 1% Triton X-100 (Sigma-Aldrich) at room temperature (RT, 22℃). Slices were then incubated for 48 hr at 4℃ with primary antibodies against the apoptotic marker-cleaved caspase-3 (1:500; rabbit polyclonal; 9661, Cell signaling), neuronal marker NeuN (1:500; mouse monoclonal; MAB377, Millipore) or astrocytic marker GFAP (1:1500; rabbit polyclonal; Z0334, Dako). Slices were incubated for 2 hr at RT with secondary antibody Alexa 546 goat anti-rabbit (1:300, A11035, Invitrogen), Alexa 647 goat anti-mouse (1:300, A21235, Invitrogen) or Cy2 donkey anti-rabbit (711-225-152, Jackson Immuno Research). Primary and secondary antibodies were diluted in PBS containing

2% NGS or 2% NDS and 0.2% Triton X-100. After staining, brain slices were mounted with Fluoroshield Mounting Medium (ab104135, Abcam).

For Htt staining, brains were embedded in tissue tek (Sakura) and frozen on dry ice with 100% ethanol. 5 – 10 μm sagittal sections were sliced and subjected to antigen retrieval by being placed in 10 mM sodium citrate buffer at 84°C or 90 – 95°C for 15 – 20 min and rinsed with TBS-Triton-X (0.3%, Roth). Subsequently, sections were blocked with 20% sheep or horse serum in TBS-Triton-X for 1 hr at RT. Primary antibody (Htt: 1:200, rabbit monoclonal, ab109115, Abcam) was diluted in TBS-Triton-X and incubated overnight at 4°C. Secondary antibody (1:200, goat anti-rabbit AlexaFluor 488, A11008, Life technologies) in TBS-Triton-X was incubated for 2 hr at RT. Afterwards, sections were embedded in fluoromount (Sigma-Aldrich) including Hoechst33342 (1:1000, B2261, Sigma-Aldrich). Mounted slices were analyzed with a confocal laser-scanning microscope (Leica SP8).

Sample preparation for respirometry experiments

Experimental animals were sacrificed by cervical dislocation immediately before OXPHOS analysis. Brains were micro-dissected on ice and specimens weighed on an analytical balance (Sartorius, CPA1003S; Germany). The micro-dissected brain regions were directly transferred into ice-cold mitochondrial respiration medium MiR05 (EGTA 0.5 mM, $MgCl_2$ 3 mM, K-lactobionate 60 mM, taurine 20 mM, KH_2PO_4 10 mM, HEPES 20 mM, sucrose 110 mM, BSA 1 g/L, adjusted to pH 7.1) (*Kuznetsov et al., 2000*). The tissue was then homogenized in a pre-cooled 1.5 ml tube with a motorized pestle in MiR05 medium with 10 strokes. Resulting homogenates containing 10 mg tissue wet weight were suspended in 100 μl of ice-cold MiR05 and later 20 μl (2 mg) from the 100 μl tissue suspension was added to each chamber of the Oxygraph-2k, Oroboros Instrument containing 2 ml of MiR05 for OXPHOS analysis (*Holmström et al., 2012*). All chemicals were purchased from Sigma-Aldrich, Germany. The optimized motorized pestle preparation of brain tissue yields a high degree of permeabilization as evident by the minimal effect of digitonin titrations on OXPHOS capacity. Therefore, digitonin is not necessary for this protocol.

High-resolution respirometry in tissue

Tissue homogenates were transferred into calibrated Oxygraph-2k (O2k, Oroboros Instruments, Innsbruck, Austria) 2 ml chambers. Oxygen polarography was performed at 37 ± 0.001°C (electronic Peltier regulation) in O2k chambers and oxygen concentration (μM) as well as oxygen flux per tissue mass (pmol $O_2 \cdot s^{-1} \cdot mg^{-1}$) were recorded real-time using DatLab software (Oroboros Instruments Innsbruck, Austria). A multisubstrate protocol was used to sequentially explore the various components of mitochondrial respiratory capacity. The homogenate was suspended in MiR05, added to the Oxygraph-2k glass chambers and the O_2 flux was allowed to stabilize. A substrate-uncoupler-inhibitor titration (SUIT) protocol was applied to assess qualitative and quantitative mitochondrial changes in Hdh150 transgenic mice and unaffected controls. After stabilization, LEAK respiration was evaluated by adding the complex I (CI) substrates malate (2 mM), pyruvate (10 mM) and glutamate (20 mM). The maximum oxidative phosphorylation (OXPHOS) capacity with CI substrates was attained by the addition of ADP+Mg^{2+} (5 mM) (CI_{OXPHOS}). For evaluation of maximum OXPHOS capacity of the convergent input from CI and complex II (CII) at saturating ADP-concentration, the CII substrate succinate (10 mM) was added (CI +CII_{OXPHOS}). We then uncoupled respiration to examine the maximal capacity of the electron transport system (ETS or CI +II_{ETS}) using the protonophore, carbonylcyanide 4 (trifluoromethoxy) phenylhydrazone (FCCP; successive titrations of 0.2 μM until maximal respiration rates were reached). We then examined consumption in the uncoupled state solely due to the activity of complex II by inhibiting complex I with the addition of rotenone (0.1 μM; ETS CII or CII_{ETS}). Finally, electron transport through complex II was inhibited by adding antimycin A (2 μM) to obtain the level of residual oxygen consumption (ROX) due to oxidating side reactions outside of mitochondrial respiration. The O_2 flux obtained in each step of the protocol was normalized by the wet weight of the tissue sample used for the analysis and in addition ROX was subtracted from the fluxes in each run to correct for non-mitochondrial respiration (*Hollis et al., 2015*). All respiration experiments comprise 2 – 3 counterbalanced blocks across days. All substrates and inhibitors used were obtained from Sigma.

Visual discrimination task

WT and presymptomatic VFDO Hdh150 mice (13 – 15 weeks of age) were isolated and food deprived for 24 hr. Subsequently, they were placed into an operant chamber with a touchscreen including two windows and a food dispenser on the opposite wall (Med Associates Inc; St. Albans). In order to keep animals motivated to perform the task, their daily food intake was adjusted to maintain body weight at 75 – 80% of their initial body weight during the course of the experiment. The experiment consisted of three phases:

1) mice were trained to collect a food pellet from the dispenser twice on day 1, 2) mice were trained to nose poke the touchscreen to obtain food pellet reward. They needed to collect and consume the pellet to proceed to the next trial. One daily session was either 30 min or 70 trials. The touch training was over when mice reached 70 trials on three consecutive days. 3) For the visual discrimination task, the screen presented two stimuli (pair 1: black vs. white or pair 2: black vs. grey), one correct, one false, randomly presented left or right. The mice were trained to nose poke the correct stimulus, whereupon a pellet was released. Again, they needed to collect and consume the pellet to proceed to the next trial. One daily session was either 30 min or 100 trials. The task was successful when the mice reached 70% correct trials on three consecutive days.

Open field test

Mice were not habituated to the set-up. Each mouse was removed from its home cage and put into a holding box next to the testing box. Subsequently, the mouse was put into the testing box facing the rear wall. The mice had time to explore the area for 5 min. Time in the center, which was determined as 10 cm away from each wall of the box, was measured automatically by EthoVision XT 8.5, when the center-point of the mouse moved into it.

Cell lines and filter retardation assay

For all cell lines used in this study the identity has been authenticated and mycoplasma contamination has been tested and excluded.

HEKT cell lines (ATCC, RRID:CVCL_1926) stably expressing FLAG-tagged HTT-exon 1 with either 51 or 83 CAG repeats under the control of a Tet-off promotor as well as the filter retardation assay were described previously (*Scherzinger et al., 1997*).

For the filter retardation assay cells were either transfected with a pool of MID1 specific siRNA oligonucleotides (AATTGACAGAGGAGTGTGATC, CACCGCAUCCUAGUAUCACACTT, CAGGA UUACAACUUUUAGGAATT, TTGAGTGAGCGCTATGACAAA, AAGGTGATGAGGCTTCGCAAA, TAGAACGTGATGAGTCATCAT) or non-silencing control oligonucleotides (AATTCTCCGAACGTG TCACGT) using Oligofectamine (Thermo Fisher Scientific) or treated with metformin at a final concentration of 1 mM and 2.5 mM for 24 hr. Cell lysates were soaked through a filter membrane and aggregates were detected using monoclonal anti-FLAG M2-Peroxidase (HRP) antibodies (Sigma-Aldrich). Signals were quantified using the Fiji Software.

FRAP (fluorescence recovery after photobleaching)-based assay

Neuro-2A (a mouse neuroblastoma cell line, ATCC, RRID:CVCL_0470) cells or murine primary cortical neurons (prepared from NMRI mice E14.5 as described previously [*Kickstein et al., 2010*] were transfected with constructs expressing Htt exon1 with 49CAG repeats fused to GFP (vector pEGFP-C1-HTTex1; an N-terminal GFP tag) the day before analysis. Cells were analyzed in a previously established FRAP-based assay to monitor translation in living cells (*Krauss et al., 2013*) using a Zeiss LSM700 confocal microscope. In brief, in contrast to standard FRAP, the GFP-signal of the entire cell was bleached using a 488 nm argon laser and fluorescence recovery was imaged over a time frame of 4 hr. The fluorescence signal was quantified as the sum of the pixel over the cell area, and the resulting total cell fluorescence was normalized to the post-bleach signal, which was set to 100%. Fluorescence recovery curves represent mean ± SEM of at least 35 cells.

Caenorhabditis elegans

The following *C. elegans* strains was used: strain AM141, genotype rmIs133 [unc-54p::Q40::YFP] (RRID:WB-STRAIN:AM141). AM141 worms express YFP that is linked to a polyglutamine stretch of 40 glutamines (Q40) in the muscle cells of the body wall. In the early lifetime of the worms YFP-Q40

is soluble and it aggregates gradually over time. This strain is used as a model for polyglutamine diseases like Huntington´s disease, since the 40Q represents a pathological range of the polyglutamine stretch.

For the treatment with metformin, NGM plates were seeded with OP50 bacteria and dried overnight. For heat inactivation OP50 bacteria were incubated at 70°C for 30 min. Metformin in a concentration of 5 mM, 10 mM or 500 mM was added the next day and dried again before usage. Worms were then put onto the plates and aggregates and liquid trashing were quantified after 5 days.

Nematodes were synchronized by hypochloride treatment. At day 5 of adulthood the worms were analyzed. Aggregates were counted under a fluorescence stereo microscope after anesthetizing the worms with 25 mM Levamisol on a coverslip. For each experiment 15 – 20 animals were counted. In addition, liquid thrashing was analyzed in 10 – 15 animals per experiment. Therefore, single worms were transferred into one drop of M9 buffer (3 g KH_2PO_4, 6 g Na_2HPO_4, 5 g NaCl, 1 ml 1 M $MgSO_4$, H_2O to 1 liter) and the rhythmic bending of the worm around its body axis was counted for 30 s. Each experiment was conducted at least three times.

Western blots

For western blotting mice were sacrificed and brains were grinded and shaked in magic mix (48% urea, 15 mM TRIS-HCl (pH7.5), 8.7% glycerin, 1% SDS, 1% mercaptoethanol, complete protease inhibitors (Roche), Phosstop (Roche) at 4°C with add-on homogenization (QIAshredder). Afterwards, samples were boiled at 95°C and 30 µg protein lysate (40 µg for Htt blot) was loaded on a 10% SDS PAGE gel, resolved (overnight at 100 V for separation of mHtt from wtHtt) and blotted onto a PVDF membrane (BioRad) using TransBlot Turbo (BioRad). Membranes were then blocked with 1% BSA (pS6) or 5% milk (Actin, Gapdh, Htt) in PBS-Tween20 (Roth) and incubated with primary antibody (Actin: 1:2000, A2066, Sigma Aldrich; pS6: 1:2000, 2215, cell signaling; Gapdh: 1:2000, ab8245, abcam; Htt: 1:850, ab109115, abcam) in blocking buffer overnight. Membranes were then washed three times with PBS-Tween20 and subsequently incubated with secondary antibody (1:6000, for Htt 1:4000, Donkey anti-rabbit or anti-mouse, Jackson Immuno Research) for 1 hr in blocking buffer. Subsequently, membranes were again washed three times with PBS-Tween20. Chemiluminescent detection was done by using Western Lightning Plus-ECL (PerkinElmer). Visualisation was performed on a ChemiDoc MP Imaging System (Biorad). Quantification of resulting bands was performed using Image Lab (version 5.2.1).

Metformin treatment in vivo

Both the Hdh150 and WT mice received chronic metformin (MP Biomedicals, LLC; France) administration (5 mg/ml in the drinking water) freshly prepared every day for 3 weeks starting from an age of 9 – 10 weeks.

Statistics

Statistical significance was tested in GraphPad Prism (GraphPad Software Inc., La Jolla, CA). *Table 1* contains all details concerning statistical tests used (name of the test, p-values, F values and degree of freedom). $*p<0.05$, $**p<0.01$, $***p<0.001$ and $****p<0.0001$. For all data, we first tested for normal distribution using the one-sample Kolmogorov-Smirnov test. In case that the null hypothesis of a normal distribution could not be rejected (for $p>0.05$), we employed a parametric test, if H_0 could be rejected (for $p<0.05$) we used non-parametric tests: Mann-Whitney U test for non-parametric data and t test for parametric data. Pearson's correlation coefficient was used on raster plots that were temporally binned (328 ms per bin) to compare activity patterns between pairs of neurons. Box-and-whisker plots indicate the median (line) of average values from multiple time-lapses, the 25-75th percentiles (box) and the 10-90th percentiles (whiskers). Graphs show mean ±s.e.m (standard error of the mean).

Data availability

Values used in figures are available on Dryad Digital repository (doi:10.5061/dryad.g3b5272) and the code used for the analysis of calcium imaging is in *Figure 1—source data 2*.

Acknowledgement

Additional information

Funding

Author contributions

Isabelle Arnoux, Michael Willam, Data curation, Formal analysis, Investigation, Visualization, Writing—original draft, Writing—review and editing; Nadine Griesche, Data curation, Formal analysis, Investigation, Visualization, Writing—original draft; Jennifer Krummeich, Investigation; Hirofumi Watari, Data curation, Software, Formal analysis, Methodology, Writing—original draft; Nina Offermann, Stephanie Weber, Formal analysis, Investigation; Partha Narayan Dey, Data curation, Formal analysis, Investigation, Visualization; Changwei Chen, Olivia Monteiro, Data curation, Formal analysis, Methodology; Sven Buettner, Katharina Meyer, Daniele Bano, Data curation, Formal analysis, Investigation; Konstantin Radyushkin, Resources, Formal analysis, Supervision, Methodology; Rosamund Langston, Formal analysis, Supervision, Methodology; Jeremy J Lambert, Supervision, Methodology; Erich Wanker, Data curation, Supervision; Axel Methner, Conceptualization, Data curation, Formal analysis, Supervision, Funding acquisition, Writing—original draft, Writing—review and editing; Sybille Krauss, Conceptualization, Data curation, Formal analysis, Supervision, Investigation, Writing—original draft, Writing—review and editing; Susann Schweiger, Albrecht Stroh, Conceptualization, Data curation, Supervision, Funding acquisition, Writing—original draft, Writing—review and editing

Author ORCIDs

Isabelle Arnoux ID http://orcid.org/0000-0003-4530-9944
Erich Wanker ID http://orcid.org/0000-0001-8072-1630
Axel Methner ID https://orcid.org/0000-0002-8774-0057
Albrecht Stroh ID http://orcid.org/0000-0001-9410-4086

Ethics

Animal experimentation: All experimental procedures were performed in accordance with institutional animal welfare guidelines and were approved by the state government of Rhineland-Palatinate, Germany (G14-1-010 and G14-1-017).

Decision letter and Author response

Decision letter https://doi.org/10.7554/eLife.38744.031

Author response https://doi.org/10.7554/eLife.38744.032

Additional files

Supplementary files

• Transparent reporting form
DOI: https://doi.org/10.7554/eLife.38744.027

Data availability

Values used in figures are available on Dryad Digital repository (doi:10.5061/dryad.g3b5272). The code used for the analysis of calcium imaging is attached as a source file. The numerical values for each figure are enclosed as source data files.

The following dataset was generated:

Author(s)	Year	Dataset title	Dataset URL	Database, license, and accessibility information
Arnoux I, Willam M, Griesche N, Krummeich J, Watari H, Offermann N, Weber S, Narayan Dey P, Chen C, Monteiro O, Buettner S, Meyer K, Bano D, Radyushkin K, Langston R, Lambert JJ, Wanker E, Methner A, Krauss S, Schweiger S, Stroh A	2018	Data from: Metformin reverses early cortical network dysfunction and behavior changes in Huntington's disease	https://dx.doi.org/10.5061/dryad.g3b5272	Available at Dryad Digital Repository under a CC0 Public Domain Dedication

References

Brooks S, Higgs G, Jones L, Dunnett SB. 2012. Longitudinal analysis of the behavioural phenotype in Hdh(CAG) 150 Huntington's disease knock-in mice. *Brain Research Bulletin* **88**:182–188. DOI: https://doi.org/10.1016/j.brainresbull.2010.05.004, PMID: 20457230

Busche MA, Eichhoff G, Adelsberger H, Abramowski D, Wiederhold KH, Haass C, Staufenbiel M, Konnerth A, Garaschuk O. 2008. Clusters of hyperactive neurons near amyloid plaques in a mouse model of Alzheimer's disease. *Science* **321**:1686–1689. DOI: https://doi.org/10.1126/science.1162844, PMID: 18802001

Busche MA, Chen X, Henning HA, Reichwald J, Staufenbiel M, Sakmann B, Konnerth A. 2012. Critical role of soluble amyloid-β for early hippocampal hyperactivity in a mouse model of Alzheimer's disease. *PNAS* **109**: 8740–8745. DOI: https://doi.org/10.1073/pnas.1206171109, PMID: 22592800

Busche MA, Kekuš M, Adelsberger H, Noda T, Förstl H, Nelken I, Konnerth A. 2015. Rescue of long-range circuit dysfunction in Alzheimer's disease models. *Nature Neuroscience* **18**:1623–1630. DOI: https://doi.org/10.1038/nn.4137, PMID: 26457554

Busche MA, Konnerth A. 2016. Impairments of neural circuit function in Alzheimer's disease. *Philosophical Transactions of the Royal Society B: Biological Sciences* **371**:20150429. DOI: https://doi.org/10.1098/rstb.2015.0429

Cabreiro F, Au C, Leung KY, Vergara-Irigaray N, Cochemé HM, Noori T, Weinkove D, Schuster E, Greene ND, Gems D. 2013. Metformin retards aging in C. elegans by altering microbial folate and methionine metabolism. *Cell* **153**:228–239. DOI: https://doi.org/10.1016/j.cell.2013.02.035, PMID: 23540700

Cepeda C, Hurst RS, Calvert CR, Hernández-Echeagaray E, Nguyen OK, Jocoy E, Christian LJ, Ariano MA, Levine MS. 2003. Transient and progressive electrophysiological alterations in the corticostriatal pathway in a mouse model of Huntington's disease. *The Journal of Neuroscience* **23**:961–969. DOI: https://doi.org/10.1523/JNEUROSCI.23-03-00961.2003, PMID: 12574425

Clabough EB. 2013. Huntington's disease: the past, present, and future search for disease modifiers. *The Yale Journal of Biology and Medicine* **86**:217–233. PMID: 23766742

Crook ZR, Housman D. 2011. Huntington's disease: can mice lead the way to treatment? *Neuron* **69**:423–435. DOI: https://doi.org/10.1016/j.neuron.2010.12.035, PMID: 21315254

Damiano M, Galvan L, Déglon N, Brouillet E. 2010. Mitochondria in Huntington's disease. *Biochimica Et Biophysica Acta (BBA) - Molecular Basis of Disease* **1802**:52–61. DOI: https://doi.org/10.1016/j.bbadis.2009.07.012

Demir U, Koehler A, Schneider R, Schweiger S, Klocker H. 2014. Metformin anti-tumor effect via disruption of the MID1 translational regulator complex and AR downregulation in prostate cancer cells. *BMC Cancer* **14**:52. DOI: https://doi.org/10.1186/1471-2407-14-52, PMID: 24484909

Dietrich P, Johnson IM, Alli S, Dragatsis I. 2017. Elimination of huntingtin in the adult mouse leads to progressive behavioral deficits, bilateral thalamic calcification, and altered brain iron homeostasis. *PLOS Genetics* **13**: e1006846. DOI: https://doi.org/10.1371/journal.pgen.1006846, PMID: 28715425

DiFiglia M, Sena-Esteves M, Chase K, Sapp E, Pfister E, Sass M, Yoder J, Reeves P, Pandey RK, Rajeev KG, Manoharan M, Sah DW, Zamore PD, Aronin N. 2007. Therapeutic silencing of mutant huntingtin with siRNA attenuates striatal and cortical neuropathology and behavioral deficits. *PNAS* **104**:17204–17209. DOI: https://doi.org/10.1073/pnas.0708285104, PMID: 17940007

Dogan I, Eickhoff SB, Schulz JB, Shah NJ, Laird AR, Fox PT, Reetz K. 2013. Consistent neurodegeneration and its association with clinical progression in Huntington's disease: a coordinate-based meta-analysis. *Neurodegenerative Diseases* **12**:23–35. DOI: https://doi.org/10.1159/000339528, PMID: 22922585

Dombeck DA, Graziano MS, Tank DW. 2009. Functional clustering of neurons in motor cortex determined by cellular resolution imaging in awake behaving mice. *Journal of Neuroscience* **29**:13751–13760. DOI: https://doi.org/10.1523/JNEUROSCI.2985-09.2009, PMID: 19889987

Dragatsis I, Levine MS, Zeitlin S. 2000. Inactivation of Hdh in the brain and testis results in progressive neurodegeneration and sterility in mice. *Nature Genetics* **26**:300–306. DOI: https://doi.org/10.1038/81593, PMID: 11062468

Duan W, Jiang M, Jin J. 2014. Metabolism in HD: still a relevant mechanism? *Movement Disorders* **29**:1366–1374. DOI: https://doi.org/10.1002/mds.25992, PMID: 25124273

Frank S. 2014. Treatment of Huntington's disease. *Neurotherapeutics* **11**:153–160. DOI: https://doi.org/10.1007/s13311-013-0244-z, PMID: 24366610

Gantois I, Khoutorsky A, Popic J, Aguilar-Valles A, Freemantle E, Cao R, Sharma V, Pooters T, Nagpal A, Skalecka A, Truong VT, Wiebe S, Groves IA, Jafarnejad SM, Chapat C, McCullagh EA, Gamache K, Nader K, Lacaille JC, Gkogkas CG, et al. 2017. Metformin ameliorates core deficits in a mouse model of fragile X syndrome. *Nature Medicine* **23**:674–677. DOI: https://doi.org/10.1038/nm.4335, PMID: 28504725

Grienberger C, Konnerth A. 2012. Imaging calcium in neurons. *Neuron* **73**:862–885. DOI: https://doi.org/10.1016/j.neuron.2012.02.011, PMID: 22405199

Griesche N, Schilling J, Weber S, Rohm M, Pesch V, Matthes F, Auburger G, Krauss S. 2016. Regulation of mRNA translation by MID1: a common mechanism of expanded CAG repeat RNAs. *Frontiers in Cellular Neuroscience* **10**:226. DOI: https://doi.org/10.3389/fncel.2016.00226, PMID: 27774050

Harper SQ, Staber PD, He X, Eliason SL, Martins IH, Mao Q, Yang L, Kotin RM, Paulson HL, Davidson BL. 2005. RNA interference improves motor and neuropathological abnormalities in a Huntington's disease mouse model. *PNAS* **102**:5820–5825. DOI: https://doi.org/10.1073/pnas.0501507102, PMID: 15811941

HD iPSC Consortium. 2017. Developmental alterations in Huntington's disease neural cells and pharmacological rescue in cells and mice. *Nature Neuroscience* **20**:648–660. DOI: https://doi.org/10.1038/nn.4532, PMID: 28319609

Heng MY, Tallaksen-Greene SJ, Detloff PJ, Albin RL. 2007. Longitudinal evaluation of the Hdh(CAG)150 knock-in murine model of Huntington's disease. *Journal of Neuroscience* **27**:8989–8998. DOI: https://doi.org/10.1523/JNEUROSCI.1830-07.2007, PMID: 17715336

Hervás D, Fornés-Ferrer V, Gómez-Escribano AP, Sequedo MD, Peiró C, Millán JM, Vázquez-Manrique RP. 2017. Metformin intake associates with better cognitive function in patients with Huntington's disease. *PLoS One* **12**: e0179283. DOI: https://doi.org/10.1371/journal.pone.0179283, PMID: 28632780

Hollis F, van der Kooij MA, Zanoletti O, Lozano L, Cantó C, Sandi C. 2015. Mitochondrial function in the brain links anxiety with social subordination. *PNAS* **112**:15486–15491. DOI: https://doi.org/10.1073/pnas.1512653112, PMID: 26621716

Holmström MH, Iglesias-Gutierrez E, Zierath JR, Garcia-Roves PM. 2012. Tissue-specific control of mitochondrial respiration in obesity-related insulin resistance and diabetes. *American Journal of Physiology-Endocrinology and Metabolism* **302**:E731–E739. DOI: https://doi.org/10.1152/ajpendo.00159.2011, PMID: 22252943

Humbert S. 2010. Is Huntington disease a developmental disorder? *EMBO Reports* **11**:899. DOI: https://doi.org/10.1038/embor.2010.182, PMID: 21102640

Iaccarino HF, Singer AC, Martorell AJ, Rudenko A, Gao F, Gillingham TZ, Mathys H, Seo J, Kritskiy O, Abdurrob F, Adaikkan C, Canter RG, Rueda R, Brown EN, Boyden ES, Tsai LH. 2016. Gamma frequency entrainment attenuates amyloid load and modifies microglia. *Nature* **540**:230–235. DOI: https://doi.org/10.1038/nature20587, PMID: 27929004

Jin J, Gu H, Anders NM, Ren T, Jiang M, Tao M, Peng Q, Rudek MA, Duan W. 2016. Metformin protects cells from mutant huntingtin toxicity through activation of AMPK and modulation of mitochondrial dynamics. *NeuroMolecular Medicine* **18**:581–592. DOI: https://doi.org/10.1007/s12017-016-8412-z, PMID: 27225841

Jin YN, Johnson GV. 2010. The interrelationship between mitochondrial dysfunction and transcriptional dysregulation in Huntington disease. *Journal of Bioenergetics and Biomembranes* **42**:199–205. DOI: https://doi.org/10.1007/s10863-010-9286-7, PMID: 20556492

Keiser MS, Kordasiewicz HB, McBride JL. 2016. Gene suppression strategies for dominantly inherited neurodegenerative diseases: lessons from Huntington's disease and spinocerebellar ataxia. *Human Molecular Genetics* **25**:R53–R64. DOI: https://doi.org/10.1093/hmg/ddv442

Kerr JN, Greenberg D, Helmchen F. 2005. Imaging input and output of neocortical networks in vivo. *PNAS* **102**: 14063–14068. DOI: https://doi.org/10.1073/pnas.0506029102, PMID: 16157876

Kerschbamer E, Biagioli M. 2015. Huntington's disease as neurodevelopmental disorder: altered chromatin regulation, coding, and non-coding RNA transcription. *Frontiers in Neuroscience* **9**:509. DOI: https://doi.org/10.3389/fnins.2015.00509, PMID: 26793052

Keskin AD, Kekuš M, Adelsberger H, Neumann U, Shimshek DR, Song B, Zott B, Peng T, Förstl H, Staufenbiel M, Nelken I, Sakmann B, Konnerth A, Busche MA. 2017. BACE inhibition-dependent repair of Alzheimer's pathophysiology. *PNAS* **114**:8631–8636. DOI: https://doi.org/10.1073/pnas.1708106114, PMID: 28739891

Kickstein E, Krauss S, Thornhill P, Rutschow D, Zeller R, Sharkey J, Williamson R, Fuchs M, Köhler A, Glossmann H, Schneider R, Sutherland C, Schweiger S. 2010. Biguanide metformin acts on tau phosphorylation via mTOR/protein phosphatase 2A (PP2A) signaling. *PNAS* **107**:21830–21835. DOI: https://doi.org/10.1073/pnas.0912793107, PMID: 21098287

Kordasiewicz HB, Stanek LM, Wancewicz EV, Mazur C, McAlonis MM, Pytel KA, Artates JW, Weiss A, Cheng SH, Shihabuddin LS, Hung G, Bennett CF, Cleveland DW. 2012. Sustained therapeutic reversal of Huntington's disease by transient repression of huntingtin synthesis. *Neuron* **74**:1031–1044. DOI: https://doi.org/10.1016/j.neuron.2012.05.009, PMID: 22726834

Krauss S, Griesche N, Jastrzebska E, Chen C, Rutschow D, Achmüller C, Dorn S, Boesch SM, Lalowski M, Wanker E, Schneider R, Schweiger S. 2013. Translation of HTT mRNA with expanded CAG repeats is regulated by the MID1-PP2A protein complex. *Nature Communications* **4**:1511. DOI: https://doi.org/10.1038/ncomms2514, PMID: 23443539

Kuznetsov AV, Brandacher G, Steurer W, Margreiter R, Gnaiger E. 2000. Isolated rat heart mitochondria and whole rat heart as models for mitochondrial cold ischemia-reperfusion injury. *Transplantation Proceedings* **32**:45. DOI: https://doi.org/10.1016/S0041-1345(99)00869-6, PMID: 10700961

Labbadia J, Morimoto RI. 2013. Huntington's disease: underlying molecular mechanisms and emerging concepts. *Trends in Biochemical Sciences* **38**:378–385. DOI: https://doi.org/10.1016/j.tibs.2013.05.003, PMID: 23768628

Labuschagne I, Cassidy AM, Scahill RI, Johnson EB, Rees E, O'Regan A, Queller S, Frost C, Leavitt BR, Dürr A, Roos R, Owen G, Borowsky B, Tabrizi SJ, Stout JC, TRACK-HD Investigators. 2016. Visuospatial processing deficits linked to posterior brain regions in premanifest and early stage Huntington's Disease. *Journal of the International Neuropsychological Society* **22**:595–608. DOI: https://doi.org/10.1017/S1355617716000321, PMID: 27211109

Lin CH, Tallaksen-Greene S, Chien WM, Cearley JA, Jackson WS, Crouse AB, Ren S, Li XJ, Albin RL, Detloff PJ. 2001. Neurological abnormalities in a knock-in mouse model of Huntington's disease. *Human Molecular Genetics* **10**:137–144. DOI: https://doi.org/10.1093/hmg/10.2.137, PMID: 11152661

Lu XH, Yang XW. 2012. "Huntingtin holiday": progress toward an antisense therapy for Huntington's disease. *Neuron* **74**:964–966. DOI: https://doi.org/10.1016/j.neuron.2012.06.001, PMID: 22726826

Ma TC, Buescher JL, Oatis B, Funk JA, Nash AJ, Carrier RL, Hoyt KR. 2007. Metformin therapy in a transgenic mouse model of Huntington's disease. *Neuroscience Letters* **411**:98–103. DOI: https://doi.org/10.1016/j.neulet.2006.10.039, PMID: 17110029

Mehler MF, Gokhan S. 2000. Mechanisms underlying neural cell death in neurodegenerative diseases: alterations of a developmentally-mediated cellular rheostat. *Trends in Neurosciences* **23**:599–605. DOI: https://doi.org/10.1016/S0166-2236(00)01705-7, PMID: 11137149

Menalled L, El-Khodor BF, Patry M, Suárez-Fariñas M, Orenstein SJ, Zahasky B, Leahy C, Wheeler V, Yang XW, MacDonald M, Morton AJ, Bates G, Leeds J, Park L, Howland D, Signer E, Tobin A, Brunner D. 2009. Systematic behavioral evaluation of Huntington's disease transgenic and knock-in mouse models. *Neurobiology of Disease* **35**:319–336. DOI: https://doi.org/10.1016/j.nbd.2009.05.007, PMID: 19464370

Micic D, Cvijovic G, Trajkovic V, Duntas LH, Polovina S. 2011. Metformin: its emerging role in oncology. *Hormones* **10**:5–15. DOI: https://doi.org/10.14310/horm.2002.1288, PMID: 21349801

Miller JE, Ayzenshtat I, Carrillo-Reid L, Yuste R. 2014. Visual stimuli recruit intrinsically generated cortical ensembles. *PNAS* **111**:E4053–E4061. DOI: https://doi.org/10.1073/pnas.1406077111, PMID: 25201983

Mochel F, Haller RG. 2011. Energy deficit in Huntington disease: why it matters. *Journal of Clinical Investigation* **121**:493–499. DOI: https://doi.org/10.1172/JCI45691, PMID: 21285522

Molero AE, Arteaga-Bracho EE, Chen CH, Gulinello M, Winchester ML, Pichamoorthy N, Gokhan S, Khodakhah K, Mehler MF. 2016. Selective expression of mutant huntingtin during development recapitulates characteristic features of Huntington's disease. *PNAS* **113**:5736–5741. DOI: https://doi.org/10.1073/pnas.1603871113, PMID: 27140644

Morley JF, Brignull HR, Weyers JJ, Morimoto RI. 2002. The threshold for polyglutamine-expansion protein aggregation and cellular toxicity is dynamic and influenced by aging in Caenorhabditis elegans. *PNAS* **99**:10417–10422. DOI: https://doi.org/10.1073/pnas.152161099, PMID: 12122205

Neueder A, Landles C, Ghosh R, Howland D, Myers RH, Faull RLM, Tabrizi SJ, Bates GP. 2017. The pathogenic exon 1 HTT protein is produced by incomplete splicing in Huntington's disease patients. *Scientific Reports* **7**:1307. DOI: https://doi.org/10.1038/s41598-017-01510-z, PMID: 28465506

Nguyen HP, Kobbe P, Rahne H, Wörpel T, Jäger B, Stephan M, Pabst R, Holzmann C, Riess O, Korr H, Kántor O, Petrasch-Parwez E, Wetzel R, Osmand A, von Hörsten S. 2006. Behavioral abnormalities precede neuropathological markers in rats transgenic for Huntington's disease. *Human Molecular Genetics* **15**:3177–3194. DOI: https://doi.org/10.1093/hmg/ddl394, PMID: 16984963

Paxinos G, Franklin KBJ. 2001. *The Mouse Brain in Stereotaxic Coordinates.* 2nd ed XXV. San Diego: Academic Press.

Pouladi MA, Morton AJ, Hayden MR. 2013. Choosing an animal model for the study of Huntington's disease. *Nature Reviews Neuroscience* **14**:708–721. DOI: https://doi.org/10.1038/nrn3570, PMID: 24052178

Predict-HD Investigators of the Huntington Study Group, Duff K, Paulsen JS, Beglinger LJ, Langbehn DR, Stout JC. 2007. Psychiatric symptoms in Huntington's disease before diagnosis: the predict-HD study. *Biological Psychiatry* **62**:1341–1346. DOI: https://doi.org/10.1016/j.biopsych.2006.11.034, PMID: 17481592

PREDICT-HD investigators of the Huntington Study Group, Harrington DL, Rubinov M, Durgerian S, Mourany L, Reece C, Koenig K, Bullmore E, Long JD, Paulsen JS, Rao SM. 2015. Network topology and functional connectivity disturbances precede the onset of Huntington's disease. *Brain* **138**:2332–2346. DOI: https://doi.org/10.1093/brain/awv145, PMID: 26059655

Putcha D, Brickhouse M, O'Keefe K, Sullivan C, Rentz D, Marshall G, Dickerson B, Sperling R. 2011. Hippocampal hyperactivation associated with cortical thinning in Alzheimer's disease signature regions in non-demented elderly adults. *Journal of Neuroscience* **31**:17680–17688. DOI: https://doi.org/10.1523/JNEUROSCI.4740-11.2011, PMID: 22131428

Ross CA, Aylward EH, Wild EJ, Langbehn DR, Long JD, Warner JH, Scahill RI, Leavitt BR, Stout JC, Paulsen JS, Reilmann R, Unschuld PG, Wexler A, Margolis RL, Tabrizi SJ. 2014. Huntington disease: natural history, biomarkers and prospects for therapeutics. *Nature Reviews Neurology* **10**:204–216. DOI: https://doi.org/10.1038/nrneurol.2014.24, PMID: 24614516

Rubinsztein DC, Orr HT. 2016. Diminishing return for mechanistic therapeutics with neurodegenerative disease duration?: there may be a point in the course of a neurodegenerative condition where therapeutics targeting disease-causing mechanisms are futile. *BioEssays : News and Reviews in Molecular, Cellular and Developmental Biology* **38**:977–980. DOI: https://doi.org/10.1002/bies.201600048, PMID: 27479863

Sathasivam K, Neueder A, Gipson TA, Landles C, Benjamin AC, Bondulich MK, Smith DL, Faull RL, Roos RA, Howland D, Detloff PJ, Housman DE, Bates GP. 2013. Aberrant splicing of HTT generates the pathogenic exon 1 protein in Huntington disease. *PNAS* **110**:2366–2370. DOI: https://doi.org/10.1073/pnas.1221891110, PMID: 23341618

Scherzinger E, Lurz R, Turmaine M, Mangiarini L, Hollenbach B, Hasenbank R, Bates GP, Davies SW, Lehrach H, Wanker EE. 1997. Huntingtin-encoded polyglutamine expansions form amyloid-like protein aggregates in vitro and in vivo. *Cell* **90**:549–558. DOI: https://doi.org/10.1016/S0092-8674(00)80514-0, PMID: 9267034

Stanek LM, Sardi SP, Mastis B, Richards AR, Treleaven CM, Taksir T, Misra K, Cheng SH, Shihabuddin LS. 2014. Silencing mutant huntingtin by adeno-associated virus-mediated RNA interference ameliorates disease manifestations in the YAC128 mouse model of Huntington's disease. *Human Gene Therapy* **25**:461–474. DOI: https://doi.org/10.1089/hum.2013.200, PMID: 24484067

Stosiek C, Garaschuk O, Holthoff K, Konnerth A. 2003. In vivo two-photon calcium imaging of neuronal networks. *PNAS* **100**:7319–7324. DOI: https://doi.org/10.1073/pnas.1232232100

Stout JC, Paulsen JS, Queller S, Solomon AC, Whitlock KB, Campbell JC, Carlozzi N, Duff K, Beglinger LJ, Langbehn DR, Johnson SA, Biglan KM, Aylward EH. 2011. Neurocognitive signs in prodromal Huntington disease. *Neuropsychology* **25**:1–14. DOI: https://doi.org/10.1037/a0020937, PMID: 20919768

Sweeney MD, Sagare AP, Zlokovic BV. 2018. Blood-brain barrier breakdown in Alzheimer disease and other neurodegenerative disorders. *Nature Reviews Neurology* **14**:133–150. DOI: https://doi.org/10.1038/nrneurol.2017.188, PMID: 29377008

Tallaksen-Greene SJ, Crouse AB, Hunter JM, Detloff PJ, Albin RL. 2005. Neuronal intranuclear inclusions and neuropil aggregates in HdhCAG(150) knockin mice. *Neuroscience* **131**:843–852. DOI: https://doi.org/10.1016/j.neuroscience.2004.10.037, PMID: 15749339

Vázquez-Manrique RP, Farina F, Cambon K, Dolores Sequedo M, Parker AJ, Millán JM, Weiss A, Déglon N, Neri C. 2016. AMPK activation protects from neuronal dysfunction and vulnerability across nematode, cellular and mouse models of Huntington's disease. *Human Molecular Genetics* **25**:1043–1058. DOI: https://doi.org/10.1093/hmg/ddv513, PMID: 26681807

Walter C, Clemens LE, Müller AJ, Fallier-Becker P, Proikas-Cezanne T, Riess O, Metzger S, Nguyen HP. 2016. Activation of AMPK-induced autophagy ameliorates Huntington disease pathology in vitro. *Neuropharmacology* **108**:24–38. DOI: https://doi.org/10.1016/j.neuropharm.2016.04.041, PMID: 27133377

Wilson H, De Micco R, Niccolini F, Politis M. 2017. Molecular imaging markers to track Huntington's Disease Pathology. *Frontiers in Neurology* **8**:11. DOI: https://doi.org/10.3389/fneur.2017.00011, PMID: 28194132

Wolf RC, Sambataro F, Vasic N, Wolf ND, Thomann PA, Saft C, Landwehrmeyer GB, Orth M. 2012. Default-mode network changes in preclinical Huntington's disease. *Experimental Neurology* **237**:191–198. DOI: https://doi.org/10.1016/j.expneurol.2012.06.014, PMID: 22742947

Yamamoto A, Lucas JJ, Hen R. 2000. Reversal of neuropathology and motor dysfunction in a conditional model of Huntington's disease. *Cell* **101**:57–66. DOI: https://doi.org/10.1016/S0092-8674(00)80623-6, PMID: 10778856

Yu ZX, Li SH, Evans J, Pillarisetti A, Li H, Li XJ. 2003. Mutant huntingtin causes context-dependent neurodegeneration in mice with Huntington's disease. *The Journal of Neuroscience* **23**:2193–2202. DOI: https://doi.org/10.1523/JNEUROSCI.23-06-02193.2003, PMID: 12657678

Zu T, Duvick LA, Kaytor MD, Berlinger MS, Zoghbi HY, Clark HB, Orr HT. 2004. Recovery from polyglutamine-induced neurodegeneration in conditional SCA1 transgenic mice. *Journal of Neuroscience* **24**:8853–8861. DOI: https://doi.org/10.1523/JNEUROSCI.2978-04.2004, PMID: 15470152